

Supersensitive seismic magnetometry of white dwarfs

NICHOLAS Z. RUI ¹, JIM FULLER ¹ AND J. J. HERMES ²

¹*TAPIR, California Institute of Technology, Pasadena, CA 91125, USA*

²*Department of Astronomy, Boston University, 725 Commonwealth Ave., Boston, MA 02215, USA*

ABSTRACT

The origin of magnetic fields in white dwarfs (WDs) remains mysterious. Magnetic WDs are traditionally associated with field strengths $\gtrsim 1$ MG, set by the sensitivity of typical spectroscopic magnetic field measurements. Informed by recent developments in red giant magnetoastroseismology, we revisit the use of WD pulsations as a seismic magnetometer. WD pulsations primarily probe near-surface magnetic fields, whose effect on oscillation mode frequencies is to asymmetricize rotational multiplets and, if strong enough, suppress gravity-mode propagation altogether. The sensitivity of seismology to magnetic fields increases strongly with mode period and decreases quickly with the depth of the partial ionization-driven surface convective zone. We place upper limits for magnetic fields in 24 pulsating WDs: 20 hydrogen-atmosphere (DAV) and three helium-atmosphere (DBV) carbon–oxygen WDs, and one extremely low-mass (helium-core) pulsator. These bounds are typically ~ 1 –10 kG, although they can reach down to ~ 10 –100 G for DAVs and helium-core WDs in which lower-frequency modes are excited. Seismic magnetometry may enable new insights into the formation and evolution of WD magnetism.

Keywords: asteroseismology, white dwarfs, magnetic fields

1. INTRODUCTION

White dwarfs (WDs) are the compact remnants of low- and intermediate-mass ($\lesssim 8M_{\odot}$) stars. Although a large fraction of WDs are now known to be magnetic ($\approx 20\%$; Bagnulo & Landstreet 2021), the origins of their magnetic fields are still largely mysterious.

Magnetic fields in WDs are typically measured using Zeeman splitting of spectral absorption or emission lines (Landstreet 2014; Ferrario et al. 2015). Recent volume-limited surveys have revealed that magnetism in typical WDs (with masses $M \leq 0.75M_{\odot}$) experience a delayed onset, with both the incidence and strength of magnetism increasing at cooling ages of 2–3 Gyr (Bagnulo & Landstreet 2021, 2022). The late appearance of magnetic fields in these WDs may be due to some combination of an outward-diffusing fossil field from earlier evolutionary stages and a magnetic dynamo activated during core crystallization (Isern et al. 2017; Schreiber et al. 2021; Ginzburg et al. 2022; Blatman & Ginzburg 2024a; Fuentes et al. 2024; Blatman & Ginzburg 2024b). In contrast, strong magnetic fields occur in a large fraction ($\sim 40\%$) of ultramassive ($M \gtrsim 1.1M_{\odot}$) WDs (Bagnulo & Landstreet 2022; Kilic et al. 2023b), suggesting a merger-related origin may be responsible for some of

them (Tout et al. 2008; García-Berro et al. 2012; Briggs et al. 2018; Schneider et al. 2020). The puzzle of WD magnetism is a timely one.

In parallel with these developments, leaps and bounds have been made in the asteroseismic inference of magnetic fields in the interiors of red giants in the last few years. The propagation of buoyancy-restored gravity waves through stably stratified regions (such as in the radiative cores of red giants) is sensitive to the magnetic field. The degree to which a standing gravity wave (*g* mode) of period *P* is locally influenced by magnetism is determined by the comparison between the radial component of the magnetic field, B_r , to the critical field

$$B_{r,\text{crit}} \sim \frac{2\pi^2}{\sqrt{\ell(\ell+1)}} \frac{\sqrt{4\pi\rho}r}{NP^2}, \quad (1)$$

where ρ is the density, r is the radial coordinate, and N is the Brunt–Väisälä (buoyancy) frequency, given in Gaussian units (Fuller et al. 2015).

Magnetism (due to fields $\gtrsim 100$ kG) is thought to dampen or outright suppress dipolar oscillations in approximately one-fifth of observed red giants (García et al. 2014; Stello et al. 2016; Cantiello et al. 2016, although see Mosser et al. 2017). This magnetic suppression can occur when $B_r > B_{r,\text{crit}}$ somewhere in

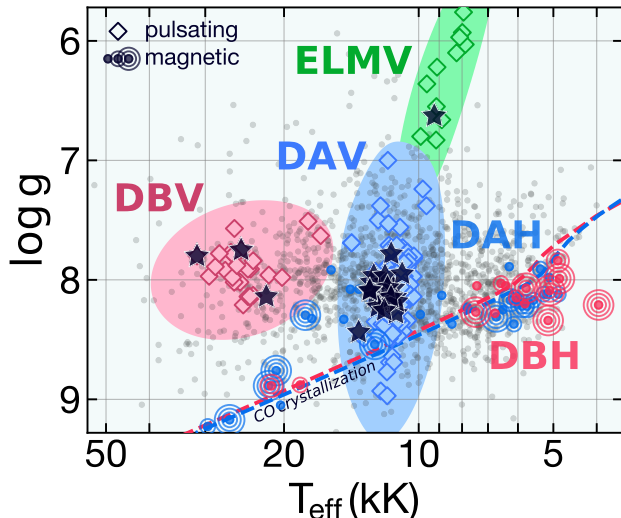


Figure 1. Kiel diagram showing various classes of pulsating (diamonds; Córscico et al. 2019) and magnetic (colored circles; Bagnulo & Landstreet 2021, 2022, with some values of $\log g$ taken from the Gaia EDR3 catalog of Gentile Fusillo et al. 2021) WDs. Black stars indicate WDs whose magnetic fields we constrain in this study, while blue points are DA WDs and red points are DB WDs from the literature. Following the plotting convention of Bagnulo & Landstreet (2022), magnetic WD points surrounded by zero, one, two, and three concentric circles have measured fields $B < 1$ MG, $1 \text{ MG} \leq B < 10 \text{ MG}$, and $10 \text{ MG} \leq B < 100 \text{ MG}$, and $B \geq 100 \text{ MG}$, respectively. The background translucent gray points indicate a subsample of other WDs in the catalog of Gentile Fusillo et al. (2021). The innermost 5% by mass of carbon–oxygen WDs with thin (thick) hydrogen envelopes will crystallize once they reach the red (blue) dashed lines (Bédard et al. 2020).

the g-mode cavity (Fuller et al. 2015; Lecoanet et al. 2017, 2022; Rui & Fuller 2023). However, in the last few years, asteroseismic frequency shifts due to weaker magnetic fields of tens to a hundred kilogauss have been detected for the very first time (Li et al. 2022; Deheuvels et al. 2023; Li et al. 2023; Hatt et al. 2024). Magnetic frequency shifts depend not only the magnetic field’s strength but also its geometry.

The majority of existing red giant magnetic field measurements based on seismic frequency shifts have relied on asymmetries in observed dipole ($\ell = 1$) triplets (Li et al. 2022, 2023). While rotation (to first order) splits a single peak in the asteroseismic power spectrum into a symmetric multiplet of $2\ell + 1$ distinct modes, the Lorentz force typically causes asymmetric splitting within the multiplet (Bugnet et al. 2021; Li et al. 2022; Das et al. 2024). Even when other sources of asymmetry cannot be excluded (e.g., near-degeneracy effects; Deheuvels et al.

2017; Ong et al. 2022), the degree (or lack) of asymmetry imposes an upper bound on the magnetic field.

The concept of performing similar, asymmetry-based magnetic field measurements in pulsating WDs dates back to Jones et al. (1989), who predicted that seismology would be sensitive to weak fields far below the “traditional” megagauss WD magnetic field. Soon after, Winget et al. (1994) reported the seismic detection of a kilogauss-level magnetic field in Whole Earth Telescope observations of the brightest DBV, GD 358 (i.e., the prototype DBV, V777 Herculis). Similar seismic field constraints have been placed on various other WDs over the years (Kawaler et al. 1995; Schmidt & Grauer 1997; Vauclair et al. 2002; Dolez et al. 2006; Fu et al. 2007; Hermes et al. 2017a), but a uniform analysis for a large sample of WDs has not been performed. Although DQVs have previously been thought to be pulsating, magnetic WDs (Dufour et al. 2008), their variability is now generally believed to be due to surface spots (Williams et al. 2016). We are not aware of any definitive detections of pulsations in known magnetic WDs.

In this work, we use asteroseismic data to place approximate upper limits on the magnetic fields in the near-surface layers of 24 WDs. In doing so, we aim to add seismology to the toolkit of WD magnetometry. Seismic magnetometry has the potential to complement traditional Zeeman effect-based techniques in constraining the formation and evolution of WD magnetic fields (Figure 1). Section 2 summarizes our present understanding of gravity waves under magnetic fields. Section 3 describes our stellar models and the procedure by which we place seismic upper bounds on WD fields. Section 4 presents and discusses our findings. Section 5 summarizes and presents optimistic prospects.

2. THEORETICAL BACKGROUND

Here, we outline the existing formalism on gravity waves under the influence of the Lorentz force. Sections 2.1 and 2.2 summarize theoretical predictions for frequency shifts and conditions for mode suppression, respectively.

The following formulae for the frequency shifts are valid in the perturbative regime where both magnetism and rotation are treated at lowest order, with the additional assumption that rotation is strong enough to set the preferred direction of the problem (see Li et al. 2022; Das et al. 2024). Mode suppression conditions arise from a non-perturbative treatment of the magnetogravity problem (e.g., Fuller et al. 2015; Lecoanet et al. 2017, 2022; Rui & Fuller 2023; Rui et al. 2024). Both calculations rely heavily on the incompressible approximation (which filters out pressure waves), the asymp-

otic approximation (which relies on high radial orders), and the Cowling approximation. Departures from these assumptions are treated in this work as an ad hoc correction factor (Appendix B). Under these assumptions, g modes are primarily sensitive to the radial component of the magnetic field B_r , and insensitive to the horizontal components B_θ and B_ϕ , which are hereafter neglected.

The aim of this work is to provide a constraint on WD field using both magnetic asymmetries and mode suppression. While both effects are primarily sensitive to the outer layers of the WD (as we subsequently explain), the exact layers probed by each effect are different, and additionally they depend on the mode period, P . Since all seismic methods we discuss probe the field in geometrically thin, near-surface layers, we speak of bounding “the” surface field B_r , which assumes that the magnetic field is roughly constant near the surface of the WD.

2.1. Seismic frequency shifts

A non-rotating, non-magnetic star such as a WD possesses spherical symmetry, so that each radial order k and angular degree ℓ are assigned to a multiplet of $2\ell + 1$ modes of varying azimuthal order $-\ell \leq m \leq \ell$ with degenerate frequencies $\nu_{n\ell}^{(0)}$. Due to geometric cancellation effects, observable g modes are typically low- ℓ , either $\ell = 1$ dipole modes or $\ell = 2$ quadrupole modes, forming mode triplets and quintuplets, respectively. The first-order effect of rotation is to split these modes into a symmetric multiplet (Ledoux 1951; Unno et al. 1979; Aerts et al. 2010; Aerts 2021):

$$\nu_{k\ell m} \approx \nu_{k\ell}^{(0)} + m \left(1 - \frac{1}{\ell(\ell + 1)} \right) \frac{\langle \Omega \rangle_g}{2\pi}, \quad (2)$$

where

$$\langle \Omega \rangle_g \approx \frac{\int_{\mathcal{R}_\nu^\ell} \Omega(N/r) dr}{\int_{\mathcal{R}_\nu^\ell} (N/r) dr} \quad (3)$$

is a wave-cavity-averaged rotation rate. The symbol \mathcal{R}_ν^ℓ denotes the g-mode cavity, the contiguous range of radii where the linear mode frequency ν satisfies $2\pi\nu < N, S_\ell$, where $S_\ell = \sqrt{\ell(\ell + 1)}c_s/r$ is the degree- ℓ Lamb frequency (Unno et al. 1979; Aerts et al. 2010). The rotational frequency shift is due to a combination of the Coriolis force (which is a physical effect) and a Doppler effect acting on the mode frequencies (which is a geometric one).

When the star is also magnetic, the magnetic tension serves as an additional, “stiffening” restorative force which shifts gravity mode frequencies by roughly

$$\begin{aligned} \nu_B^\ell &\equiv \frac{A_\ell}{64\pi^5} \frac{P^3}{\int_{\mathcal{R}_\nu^\ell} (N/r) dr} \int_{\mathcal{R}_\nu^\ell} dr \frac{N^3}{\rho r^3} \int \frac{B_r^2}{4\pi} d\Omega \\ &= A_\ell \frac{\mathcal{I}}{64\pi^5} \langle B_r^2 \rangle P^3, \end{aligned} \quad (4)$$

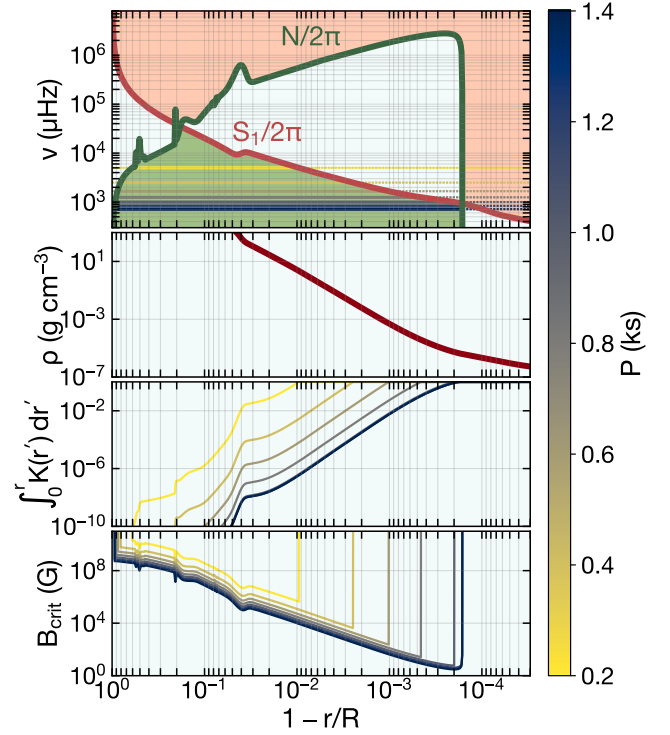


Figure 2. *Top:* Asteroseismic propagation diagram for the dipole ($\ell = 1$) modes of a WD model with $M = 0.64M_\odot$ and $T_{\text{eff}} = 12\text{ kK}$, with $1 - r/R$ on the x axis (fractional radius from the outermost shell of the model). The *green* and *brown* curves show the Brunt–Väisala (N) and dipole Lamb (S_1) frequencies, respectively. The *green shaded region* denotes the g-mode cavity. *Second from top:* Density as a function of radius. *Third from top:* Cumulative magnetic weight function (defined in Equation 7) for the same model, for a variety of mode periods. The function $\int_0^r K(r') dr'$ represents the cumulative contribution of the magnetic field in shells within radii r to the average $\langle B_r^2 \rangle$ (Equation 6). *Bottom:* Critical field $B_{r,\text{crit}}$ required to suppress gravity waves, for a variety of mode periods.

where $d\Omega$ is an integral over a spherical surface and

$$\mathcal{I} \simeq \frac{\int_{\mathcal{R}_\nu^\ell} (N^3/\rho r^3) dr}{\int_{\mathcal{R}_\nu^\ell} (N/r) dr}, \quad (5)$$

and $P = 1/\nu$ is the period of the mode and $A_\ell = \ell(\ell + 1)/2$. The characteristic scale ν_B^ℓ of the frequency shift can be computed from a field strength and stellar model (which enters Equation 4 purely through \mathcal{I}).

The weighted average $\langle B_r^2 \rangle$ which appears in Equation 4 is given by Li et al. (2022):

$$\langle B_r^2 \rangle = \int_{\mathcal{R}_\nu^\ell} dr K(r) \int \frac{d\Omega}{4\pi} B_r^2, \quad (6)$$

where the weight function is

$$K(r) \simeq \begin{cases} \frac{N^3/\rho r^3}{\int_{\mathcal{R}^\ell_\nu} (N^3/\rho r^3) dr} & \text{in } \mathcal{R}^\ell_\nu \\ 0 & \text{otherwise} \end{cases}. \quad (7)$$

The quantity ν_B^ℓ is the mean frequency shift averaged over a multiplet. However, individual modes within the multiplet will experience different frequency shifts from each other. The precise order-unity prefactor relating a mode’s magnetic frequency shift to ν_B^ℓ depends both on the quantum numbers of the mode and the geometry of the field (Li et al. 2022). As a consequence, unlike rotation, magnetism does not generically preserve the symmetry of the multiplet, and the asymmetry of the multiplet can distinguish frequency shifts due to magnetism from those due to first-order rotation.

The asymmetry of a multiplet can be parameterized by dimensionless asymmetry parameters $a_{m_1 m_2 m_3}^\ell$, the most commonly used of which (“ a ”) is defined as

$$a_{-10+1}^{\ell=1} = \frac{\Delta_{-10+1}^{\ell=1}}{3\nu_B^{\ell=1}}, \quad (8)$$

where

$$\Delta_{-10+1}^{\ell=1} = \nu_{m=-1}^{\ell=1} - 2\nu_{m=0}^{\ell=1} + \nu_{m=+1}^{\ell=1} \quad (9)$$

is a linear combination of the three dipole modes in a triplet (Li et al. 2022; Mathis & Bugnet 2023; Das et al. 2024). This is the only possible asymmetry parameter for $\ell = 1$.

We similarly construct quadrupole asymmetry parameters by taking linear combinations $\Delta_{m_1 m_2 m_3}^\ell \propto \nu_B^\ell$ of three modes within the same multiplet such that the first-order rotational splitting terms cancel out (our adopted definitions for $\Delta_{m_1 m_2 m_3}^{\ell=2}$ are given by Equations A9). We define the ten quadrupole asymmetry parameters $a_{m_1 m_2 m_3}^\ell$ as

$$a_{m_1 m_2 m_3}^\ell = \frac{\Delta_{m_1 m_2 m_3}^{\ell=2}}{5\nu_B^{\ell=2}}. \quad (10)$$

In Appendix A, we relate them to the magnetic field geometry and compute them for an inclined dipolar magnetic field (see also Das et al. 2024).

In WDs, ρ sharply decreases towards surface, and N often also reaches its peak value there, just below the surface convective zone. The weight function $K(r)$ is thus very sharply peaked just below the surface, at depths $1 - r/R \sim 10^{-3}$ – 10^{-2} , and asteroseismology is most sensitive to the near-surface field (*center panel* of Figure 2). This is in contrast to the cases of red giant or intermediate-mass main-sequence stars, within which $K(r)$ peaks at some highly stratified layer in the deep interior of the star (the hydrogen-burning shell

and near-core composition gradient, respectively; Fuller et al. 2015; Lecoanet et al. 2022). While the pulsations of WDs are in principle modified by deep internal magnetic fields, the influence of these fields is highly diluted. In the $0.64M_\odot$ WD model in Figure 2, a uniform magnetic field of $\simeq 1$ MG restricted to the inner $r/R \lesssim 0.993$ of the WD affects a $P = 1200$ s gravity mode identically to a uniform $\simeq 1$ G field restricted to the outer layers with $r/R \gtrsim 0.993$. Long-period modes probe the magnetic field at very low-density layers ($\rho \simeq 4 \times 10^{-6}$ g cm $^{-3}$ for the $P = 1200$ s mode in Figure 2), although still far within the photosphere of the WD.

In principle, magnetic shifts also modify the spacing between adjacent multiplets, causing a period-dependent period spacing $\Delta\Pi_\ell = \Delta\Pi_\ell(P)$ (e.g., Cantiello et al. 2016; Rui et al. 2024). Deheuvels et al. (2023) used this effect to measure strong magnetic fields in red giants in which dipole triplets were not detected. However, this is likely difficult in WDs, whose g modes already depart from period-uniformity due to non-asymptotic mode trapping effects due to, e.g., near-surface composition gradients (Brassard et al. 1992). We instead focus on intra-multiplet asymmetries, since non-asymptotic effects are expected to affect each component of a multiplet in the same way.

2.2. Mode suppression

About $\simeq 20\%$ of observed red giants have unusually low-amplitude non-radial (dipole) oscillations (García et al. 2014; Stello et al. 2016). Fuller et al. (2015) show that the amplitudes of these suppressed oscillations are consistent with nearly total damping of g-mode oscillations in the core. They argue that such near-total suppression of g modes can occur if the damping mechanism is magnetic in nature. Simple scaling arguments (Fuller et al. 2015; Cantiello et al. 2016; Rui & Fuller 2023) show that g modes will be significantly affected by a magnetic field when the radial component of the field approaches $B_{r,\text{crit}}$ as defined in Equation 1, and detailed calculations validate several magnetic dissipation mechanisms (Lecoanet et al. 2017; Loi & Papaloizou 2017, 2018; Loi 2020; Lecoanet et al. 2022; Rui & Fuller 2023). Throughout this work, we assume that magnetic g-mode suppression damps out all g-mode energy (although see Mosser et al. 2017), and use the presence of non-suppressed g modes in WDs to set upper bounds on the magnetic field.

As can be seen in Equation 1, longer-period modes require weaker magnetic fields to suppress. At fixed ℓ , the longest-period modes observed in a WD therefore set the strongest upper limits on the WD field. Also, since $B_{r,\text{crit}} \propto \sqrt{\rho}/N$, the value of $B_{r,\text{crit}}$ reaches a minimum

near the outer edge of the WD g-mode cavity. Therefore, like magnetic asymmetries, magnetic mode suppression probes the near-surface layers. The bottom panel of Figure 2 shows $B_{r,\text{crit}}$ for various g modes in a $0.64M_{\odot}$ WD. While fields of $\simeq 3$ G at a depth of $r/R = 0.998$ are sufficient to suppress $P = 1200$ s oscillations, a $\simeq 10$ MG field is needed to achieve the same effect at a depth of $r/R = 0.9$.

For simplicity, when calculating $B_{r,\text{crit}}$, we adopt the dimensionless prefactors shown in Equation 1 originally derived by Fuller et al. (2015). In reality, this prefactor actually depends on ℓ , m , and the field geometry in complicated ways (Lecoanet et al. 2017; Loi & Papaloizou 2018; Rui & Fuller 2023). Because this prefactor is order-unity (Lecoanet et al. 2017; Rui & Fuller 2023), its uncertain value translates to order-unity errors in the inferred field strength, but changes in its value are unlikely to greatly affect the field constraint.

3. METHODS

3.1. White dwarf models

Seismic magnetic field estimates rely on detailed stellar models. To this end, we use several helium-core and carbon–oxygen WD models prepackaged with version r10398 of the Modules for Experiments in Stellar Astrophysics code (MESA; Paxton et al. 2010, 2013, 2015, 2018). We evolve models down a cooling track in the presence of gravitational settling using as diffusion representatives ^1H , ^4He , ^{12}C , ^{16}O , ^{20}Ne , and ^{22}Ne . In order to avoid helium shell flashes and/or help with numerical convergence issues, we sometimes artificially reduce the size of the hydrogen atmosphere by replacing its inner layers with helium. In one case ($M = 0.73M_{\odot}$), we replace the outer layers of the originally helium-atmosphere model with hydrogen to create a DA WD model. We also evolve several helium-atmosphere (DB) and DA WD models with lower total hydrogen masses M_{H} , initialized by replacing some of the WD’s hydrogen with helium prior to evolution.

We apply the Ledoux criterion for convective stability. This sometimes produces short-lived convective zones owing to the particular composition gradient in the initial stellar model. Although these convective zones can technically split the WD into multiple g mode cavities (requiring more sophisticated analysis Pinçon & Takata 2022), the appearance times, locations, and lifetimes of these convective zones are hard to predict. When performing integrals over the g mode cavity (i.e., when determining \mathcal{R}_{ν}^{ℓ}), we therefore integrate over all shells satisfying the gravity wave propagation condition ($2\pi\nu < N, S_{\ell}$) without enforcing that the g-mode cavity

core	type	$M (M_{\odot})$	$M_{\text{H}} (M_{\odot})$	$M_{\text{He}} (M_{\odot})$
He	DA	0.15*	9.95×10^{-4}	...
He	DA	0.20	9.54×10^{-4}	...
He	DA	0.40*	7.26×10^{-5}	...
CO	DA	0.52	8.53×10^{-5}	2.90×10^{-2}
CO	DB	0.52	0	2.91×10^{-2}
CO	DA	0.64	1.64×10^{-5}	4.23×10^{-3}
CO	DA	0.64*	8.00×10^{-8}	4.25×10^{-3}
CO	DB	0.64	0	4.25×10^{-3}
CO	DA	0.73	3.48×10^{-6}	2.53×10^{-3}
CO	DB	0.73	0	2.54×10^{-3}
CO	DA	0.86	3.99×10^{-6}	1.64×10^{-3}
CO	DB	0.86	0	1.65×10^{-2}

Table 1. Summary of the WD models used in this work (Section 3.1). Asterisks (*) indicate that we checked the magnetic sensitivity of the model, but did not use it in fitting WD observations.

is contiguous. Our WD models are summarized in Table 1.¹

3.2. Seismic field constraints

Magnetism tends to asymmetricize rotational multiplets. Symmetric multiplets therefore place upper limits on the magnetic field present in a WD. For each multiplet, we use Equations 8 (for $\ell = 1$) or 10 (for $\ell = 2$) to convert a measured asymmetry to ν_B^{ℓ} . To be conservative, we calculate this magnetic field bound assuming that the measured asymmetry is underestimated by 2σ , i.e., using as the asymmetry $|\Delta_{m_1 m_2 m_3}^{\ell}| + 2\delta\Delta_{m_1 m_2 m_3}^{\ell}$ where $\delta\Delta_{m_1 m_2 m_3}^{\ell}$ is the uncertainty on the asymmetry implied by the measurement uncertainties on the mode frequencies. Finally, we invert Equation 4 to solve for the upper limit $B_{r,\text{shift}} = \sqrt{\langle B_r^2 \rangle}$:

$$B_{r,\text{shift}} = 8\pi^{5/2} \sqrt{\min \left\{ \frac{|\Delta_{m_1 m_2 m_3}^{\ell}| + 2\delta\Delta_{m_1 m_2 m_3}^{\ell}}{|a_{m_1 m_2 m_3}^{\ell}| A_{\ell} \mathcal{I} P^3} \right\}} \quad (11)$$

where the minimum is over all combinations of three modes (indexed by m_1 , m_2 , and m_3) within the same multiplet. The quantity \mathcal{I} is corrected for non-asymptotic effects using an ad hoc factor described in Appendix B.

In this work, we assume asymmetry parameters $a_{m_1 m_2 m_3}^{\ell}$ typical for an inclined, centered dipolar magnetic field (derived in Appendix A.3). This sets $a_{-1 0 +1}^{\ell=1} \approx 0.253$ and $a_{m_1 m_2 m_3}^{\ell=2}$ to values between -0.217

¹ These MESA models can be reproduced with the inlists, `run_star_extras.f`, and other files at the following link: [to post after acceptance](#)

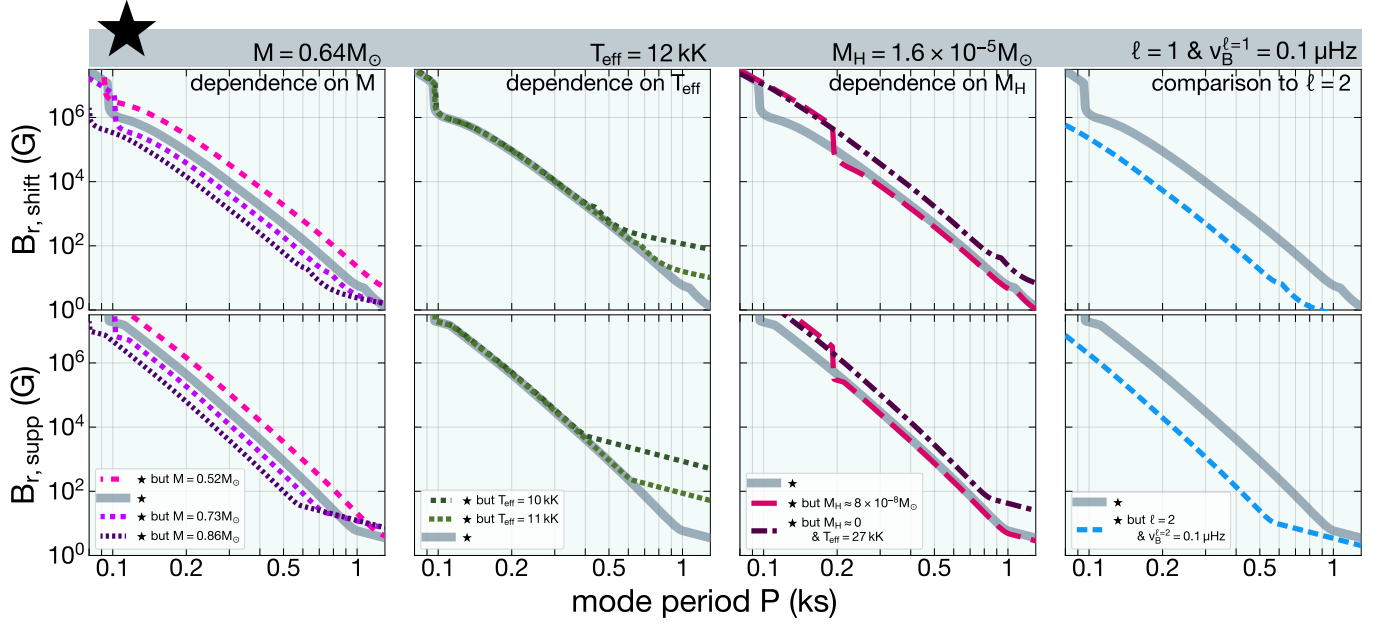


Figure 3. Model seismic magnetic field sensitivities $B_{r,\text{shift}}$ and $B_{r,\text{supp}}$. From left to right, columns show the effect of varying total mass M , effective temperature T_{eff} , hydrogen atmosphere mass M_{H} , and angular degree ℓ . These comparisons are made relative to fiducial parameters (listed in the top gray box), which we plot in gray and denote with \star . In particular, we show the value of $B_{r,\text{shift}}$ implied by a dipole multiplet with an asymmetry of $\nu_{\text{B}}^{\ell=1} = 0.1 \mu\text{Hz}$. Note that $B_{r,\text{shift}} \propto \sqrt{\nu_{\text{B}}^{\ell}}$ whereas $B_{r,\text{supp}}$ does not depend on ν_{B}^{ℓ} at all.

and -0.036 , depending on the values of m_1 , m_2 , and m_3 . While the field geometry is uncertain in reality, changes to the field geometry only modify the field strength estimate by order-unity factors. Mode asymmetries can also be non-magnetic in origin (e.g., from second-order rotational effects or near-degeneracy effects). However, we assume that other sources of asymmetry do not decrease the rough scale of the observed symmetry. In principle, we can underestimate the magnetic field if another source of asymmetry happens to nearly cancel out the magnetic asymmetry.

When $B_r > B_{r,\text{crit}}(P)$, a g mode of period P is expected to be suppressed. Therefore, the presence of a g mode indicates that the field does not exceed $B_{r,\text{crit}}$. We use this fact to place additional suppression-based upper bounds $B_{r,\text{supp}}$ by setting $B_{r,\text{supp}} = B_{r,\text{crit}}$ and inverting Equation 1 for each mode:

$$B_{r,\text{supp}} = 4\pi^{5/2} \min \left\{ \frac{(\sqrt{\rho} r/N)_{\min g, P_0}}{\sqrt{\ell(\ell+1)P_0^2}} \right\} \quad (12)$$

where the minimum is over all observed radial orders. The quantity $(\sqrt{\rho} r/N)_{\min g, P}$ is the minimum value of $\sqrt{\rho} r/N$ in the g-mode cavity corresponding to period P . The period P_0 indicates the central frequency of the multiplet, which we take as an estimate for the unperturbed mode period. When the $m = 0$ component is reported, we take its period to be P_0 . Other-

wise, if two or more components are reported, we calculate $P_0 = 1/\nu^{(0)}$, where $\nu^{(0)}$ is the y -intercept of a fit to the mode frequencies ν within a multiplet to a linear function of m . Finally, if there is only a single mode within the multiplet, we take its period as P_0 . As can be seen in Equation 1, the minimum is always set by either the longest-period dipole multiplet or longest-period quadrupole multiplet. Since this constraint relies on the *existence* of an excited radial order rather than a rotational multiplet asymmetry, we only require a single observed mode within a multiplet.

3.3. Dependence of magnetic sensitivity on white dwarf properties

The sensitivity of a WD's oscillation modes to magnetism depends on the WD's structure, particularly through \mathcal{S} (defined in Equation 5) for $B_{r,\text{shift}}$ and $(\sqrt{\rho} r/N)_{\min g, P}$ (through Equation 12) for $B_{r,\text{supp}}$.

The first three columns of Figure 3 show how $B_{r,\text{shift}}$ and $B_{r,\text{supp}}$ depend on various WD properties relative to a fiducial DAV model with $M = 0.64 M_{\odot}$ and $T_{\text{eff}} = 12 \text{ kK}$. To good approximation, both $B_{r,\text{shift}}$ (at fixed ν_{B}^{ℓ}) and $B_{r,\text{supp}}$ can be described as broken power laws, with a shallower power law index at higher mode periods. The transition period P_t between these two regimes corresponds to the mode period above (below) which the outer boundary g-mode cavity is set by N (S_{ℓ}). It is given by $P_t = 2\pi/S_{\ell}$ at the outer inter-

section between N and S_ℓ , and corresponds to a long period $P_t \simeq 1100$ s ($\nu \simeq 900 \mu\text{Hz}$) for dipole modes in the model in Figure 2 (consistent with the value computed by Montgomery et al. 2020). Hereafter, we refer to modes with long periods $P > P_t$ (short periods $P < P_t$) as N -limited (S_ℓ -limited).

The Lamb frequency S_ℓ has a gradually varying profile. This means the outer boundary of the g-mode cavity varies substantially with P for S_ℓ -limited modes. Since the layers of the WD most sensitive to magnetism are those closest to the outer boundary of the radiative zone, both $B_{r,\text{shift}}$ and $B_{r,\text{supp}}$ for S_ℓ -limited modes strongly depend on P . Conversely, the Brunt-Väisälä frequency N drops sharply at the outer boundary of the radiative zone. Accordingly, the outer g-mode-cavity boundaries of N -limited modes are essentially identical to each other. In this regime, $B_{r,\text{shift}}$ and $B_{r,\text{supp}}$ have the approximate scalings $B_{r,\text{shift}} \propto P^{-3/2}$ and $B_{r,\text{supp}} \propto P^{-2}$, reflecting only the explicit period dependences in Equations 11 and 12.

More massive WDs have higher dynamical frequencies, which in turn increases both N and S_ℓ (first column of Figure 3). In the S_ℓ -limited regime, the increased S_ℓ in more massive WDs translates to an outer g-mode cavity boundary which is closer to the surface. S_ℓ -limited modes in more massive WDs are thus more magnetically sensitive than those in less massive WDs. We find that the magnetic sensitivity of N -limited modes, however, is almost independent of mass.

The primary effect of varying the effective temperature T_{eff} (second column of Figure 3) is to change the extent of the outer, partial ionization-driven convection zone. As DA WDs cool below $T_{\text{eff}} \sim 13$ kK, they develop progressively deeper (albeit low mass; $M_{\text{conv}}/M_{\text{WD}} \sim 10^{-12}$) convective zones driven by a near-surface partial ionization zone (e.g., Tremblay et al. 2015b). The result is that both $B_{r,\text{shift}}$ and $B_{r,\text{supp}}$ are unaffected for S_ℓ -limited modes. However, N -limited modes are less sensitive to magnetic fields in cooler WDs because they are confined deeper in the WD where ρ is larger and N is smaller. Furthermore, cooler WDs have lower P_t : as they cool, the range of frequencies which are N -limited widens. While only very-long dipole period modes are N -limited in most cases, P_t drops dramatically near the very red edge of the DAV instability strip ($P_t \simeq 600$ s in the $T_{\text{eff}} = 10$ kK model in the second panel of Figure 3).

Because the near-surface partial ionization zone is also responsible for mode excitation (Brickhill 1991; Goldreich & Wu 1999), the DA instability strip contains DAVs with both deep and shallow convective zones on its red and blue sides, respectively. Deep convective zones also develop within the the DBV instability strip for similar

reasons, albeit at a hotter temperature $T_{\text{eff}} \approx 30$ kK (Fontaine & Wesemael 1987). Diminished sensitivity of long-period modes in cooler WDs (relative to hotter ones) trades off with the tendency of cooler WDs to excite more sensitive longer-period modes (e.g., Van Groenel et al. 2012; Hermes et al. 2017b).

Although hydrogen spectral lines in DA WDs indicate the presence of surface hydrogen, the precise amount of this hydrogen is very uncertain. The third column of Figure 3 shows that the effect of changing the hydrogen mass M_{H} is minor. This is because the depth of the surface convective zone is largely insensitive to M_{H} , as long as it is enough to prevent the development of a helium partial ionization-driven convection zone around $\simeq 25$ kK. Figure 3 also shows the sensitivity of a DB model in the DBV instability strip which, despite being much hotter, has a similar sensitivity to the DAV model.

At fixed ν_B^ℓ , quadrupole modes are more sensitive than dipole modes (last column in Figure 3), especially for S_ℓ -limited modes. Since $S_\ell \propto \sqrt{\ell(\ell+1)}$, the outer boundary of the g-mode cavity of S_ℓ -limited quadrupole modes is farther out than those of S_ℓ -limited dipole modes. For the same reason, P_t is significantly lower for quadrupole modes ($P_t \simeq 600$ s for the model in Figure 3).

In contrast, N -limited quadrupole modes only achieve a modest improvement in sensitivity over their dipole counterparts. In this case, both $B_{r,\text{shift}}$ and $B_{r,\text{supp}}$ are decreased by a factor of $\approx \sqrt{3}$, owing to their explicit dependences on ℓ in Equations 11 and 12.

4. SEISMIC FIELD CONSTRAINTS IN OBSERVED WHITE DWARFS

We place asymmetry- and suppression-based upper bounds on the magnetic field for 24 observed pulsating WDs of varying types (Table 2). For each WD, we first identify the stellar model which best minimizes

$$\chi^2 = \left(\frac{T_{\text{eff,spec}} - T_{\text{eff,model}}}{100 \text{ K}} \right)^2 + \left(\frac{\log g_{\text{spec}} - \log g_{\text{model}}}{0.01} \right)^2, \quad (13)$$

where $T_{\text{eff,spec}}$ and $\log g_{\text{eff,spec}}$ are spectroscopically measured values of T_{eff} and $\log g$ taken from the literature. In other words, we choose the stellar model which best matches the location of the WD on the Kiel diagram. Using this model, we then compute $B_{r,\text{shift}}$ and $B_{r,\text{supp}}$ using Equations 11 and 12. These upper bounds are shown in Table 2 and Figure 4.

4.1. Magnetic leaf diagrams

We visualize the impact of magnetism on seismology using “leaf diagrams,” such as those shown in Figure 5. For each ℓ , the leaf diagram plots as *brown circles* the

Table 2. Observed and model spectroscopic/seismic properties and upper limits on the magnetic field of 24 WDs

name	type	model M	P (ks)		T_{eff} (kK)		$\log g$		B_r upper bound (G)	
			P_{min}	P_{max}	data	model	data	model	$B_{r,\text{shift}}$	$B_{r,\text{supp}}$
GD 278 ^{1,2}	ELMV	0.20	2.29	6.73	9.23	9.33	6.63	6.65	100	70
KIC 4357037 ³	DAV	0.64	0.28	0.35	12.75	12.81	8.02	8.07	4k	10k
KIC 4552982 ³	DAV	0.73	0.36	0.36	11.24	11.15	8.28	8.24	1k	4k
KIC 7594781 ³	DAV	0.64	0.28	0.30	12.04	11.93	8.17	8.07	10k	30k
KIC 10132702 ³	DAV	0.73	0.62	0.89	12.22	12.20	8.17	8.23	8	4
KIC 11911480 ³	DAV	0.64	0.20	0.32	11.88	11.93	8.02	8.07	8k	20k
EPIC 60017836 ³	DAV	0.73	0.83	1.22	11.28	11.34	8.14	8.23	50	20
EPIC 201719578 ³	DAV	0.64	0.37	0.46	11.39	11.39	8.07	8.08	1k	2k
EPIC 201730811 ³	DAV	0.64	0.16	0.35	12.60	12.63	7.96	8.07	10k	10k
EPIC 201802933 ³	DAV	0.73	0.12	0.40	12.53	12.51	8.14	8.23	2k	2k
EPIC 201806008 ³	DAV	0.73	0.41	0.41	11.20	11.15	8.18	8.24	1k	1k
EPIC 210397465 ³	DAV	0.52	0.67	1.39	11.52	11.56	7.78	7.85	200	5
EPIC 211596649 ³	DAV	0.64	0.27	0.30	11.89	11.93	7.97	8.07	7k	30k
EPIC 211629697 ³	DAV	0.52	0.49	0.49	10.89	10.85	7.95	7.85	3k	4k
EPIC 211914185 ³	DAV	0.86	0.11	0.20	13.62	13.66	8.44	8.42	60k	80k
EPIC 211926430 ³	DAV	0.64	0.12	0.30	11.74	11.56	8.06	8.08	9k	30k
EPIC 228682478 ³	DAV	0.73	0.29	0.29	12.34	12.20	8.23	8.23	4k	10k
EPIC 229227292 ³	DAV	0.64	0.29	0.37	11.53	11.56	8.15	8.08	3k	7k
EPIC 220204626 ³	DAV	0.73	0.51	0.80	11.94	11.82	8.26	8.23	60	20
EPIC 220258806 ³	DAV	0.64	0.15	0.30	12.89	12.81	8.09	8.07	10k	30k
EPIC 220347759 ³	DAV	0.64	0.12	0.25	12.86	12.81	8.09	8.07	20k	90k
EPIC 228782059 ⁴	DBV	0.73	0.23	0.34	21.91	21.76	8.14	8.23	6k	3k
GD 358 ^{5,6}	DBV	0.52	0.42	0.77	24.94	24.86	7.75	7.83	700	500
PG 0112+104 ^{7,8}	DBV	0.52	0.15	0.50	31.30	31.30	7.80	7.80	200k	10k

For the 24 WDs for which we place a magnetic field upper limit, the WD type, model mass M , minimum P_{min} and maximum P_{max} retained pulsation period, spectroscopically measured and model T_{eff} and $\log g$, and asymmetry- and suppression-based magnetic field upper limits $B_{r,\text{shift}}$ and $B_{r,\text{supp}}$. 1: Lopez et al. (2021) 2: Calcaferro et al. (2023) 3: Hermes et al. (2017b) 4: Duan et al. (2021) 5: Winget et al. (1994) 6: Córscico et al. (2019) 7: Hermes et al. (2017a) 8: Dufour et al. (2010)

value of ν_B^ℓ implied by a measurement of the asymmetry $\Delta_{m_1 m_2 m_3}^\ell$ (Equations 8 and 10) against the mode period P . The error bars on these points denote 2σ uncertainty intervals on the asymmetries. The magnetic field required to reproduce an observed asymmetry can be read off of the diagram by comparing to the contours in the background of the leaf diagram, which show model predictions for ν_B^ℓ (from Equation 4). The *solid blue stripe* shows $B_{r,\text{shift}}$, corresponding to the weakest-field strength contour which entirely encloses the lowest asymmetry point (the one closest to the x axis), including its full error bar.

The *yellow dotted regions* show “magnetically forbidden” values of ν_B^ℓ . Observed asymmetries in this region are so high that the field required to generate them (in the perturbative theory) would also magnetically suppress the mode. Under the present assumptions, such asymmetries must therefore be non-magnetic in origin.

Accordingly, if a field contour is in the forbidden region at some period P , that magnetic field strength suppresses a g mode of period P . The boundary of the forbidden region is demarcated by ν_B^ℓ evaluated at $B_{r,\text{crit}}$. The *vertical gray lines* show the estimated central components of the multiplets, including those too incomplete for an asymmetry measurement. The suppression constraint $B_{r,\text{supp}}$ (the *dotted red stripe*) can be read off the diagram by finding the weakest-field ν_B^ℓ contour which intersects with all *vertical gray lines* before entering the forbidden region.

As defined in Equation 4, ν_B^ℓ is strictly non-negative. Negative values of ν_B^ℓ on the leaf diagram represent those where the sign of the measured asymmetry differs from the assumed sign of $a_{m_1 m_2 m_3}^\ell$ (given for this work in Appendix A.3). A negative value thus indicates an incorrect assumption about the magnetic field geometry, or a non-magnetic origin for the asymmetry altogether.

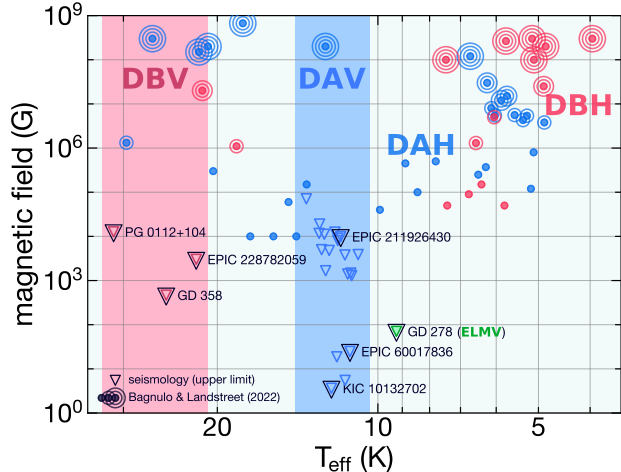


Figure 4. Seismic upper limits on WD magnetic fields $\min(B_{r,\text{shift}}, B_{r,\text{supp}})$ (triangles) versus T_{eff} , compared to the spectropolarimetric measurements (circles) of Bagnulo & Landstreet (2022). Concentric circles have the same meaning as in Figure 1. We explicitly label WDs whose leaf diagrams are shown in Figures 5, 6, and 8.

However, as $a_{m_1 m_2 m_3}^\ell$ is an order-unity constant, incorrect assumptions about its value only affect $B_{r,\text{shift}}$ by order-unity factors.

4.2. Carbon-oxygen white dwarfs

As Figure 1 shows, both the DAV and DBV WD instability strips lie blueward of both the concentration of magnetic WDs ~ 6 kK and the onset of carbon-oxygen crystallization for near-canonical masses $\simeq 0.6M_\odot$. Pulsating WDs may thus represent present-day magnetic WDs when they were younger and hotter. It takes > 2 Gyr for both our $0.64M_\odot$ DA and DB models to cool from the DAV and DBV instability strips to 6 kK.

Our sample of DAV WDs is taken from the *K2* catalog of Hermes et al. (2017b). Whenever possible, we use mode periods and uncertainties given by their nonlinear least-squares method. However, they also find that some (usually low-period; $P \gtrsim 800$ s) modes have power spectral linewidths which are significantly broader than implied by the spectral window, consistent with a lack of phase stability (see also Winget et al. 1994; Bischoff-Kim et al. 2019; Montgomery et al. 2020). In these cases, they fit a Lorentzian to the power spectral peak. When the nonlinear least-squares uncertainties are not reported, we adopt the uncertainties on the mode period derived from this Lorentzian fit.

To be conservative, we have excluded uncertain or unknown identifications of ℓ for calculating $B_{r,\text{supp}}$, as well as either ℓ or m for $B_{r,\text{shift}}$. We have also excluded all modes which are labeled as combination frequencies. This leaves 20 DAVs for which we place upper bounds

on the magnetic field. These upper bounds are usually in the range 1–10 kG, but sometimes are as low as a few gauss for DAVs within which long-period modes are excited. We show leaf diagrams for three selected DAVs in Figure 5.

Additionally, we select 3 DBVs which span the temperature range of the DBV instability strip. Using mode frequencies reported by Duan et al. (2021), we place an upper bound $B_{r,\text{shift}} \sim 3$ kG for the “cool” ($T_{\text{eff}} \approx 22$ kK) WD EPIC 228782059. We similarly place an upper bound $B_{r,\text{shift}} \sim 10$ kG for the “hot” ($T_{\text{eff}} \approx 31$ kK; Dufour et al. 2010) DBV PG 0112+104, consistent with the bound placed by Hermes et al. (2017a). The leaf diagrams of these WDs are shown in Figure 6.

As a further consistency check, we revisit GD 358, finding an asymmetry-based bound $B_{r,\text{shift}} \sim 800$ G set by the lowest-frequency triplet (similar to their inferred value ≈ 1.3 kG), as well as a formally slightly stronger suppression-based bound $B_{r,\text{supp}} \sim 500$ G. Curiously, subsequent observations of GD 358 have observed time variation in both the amplitudes and frequencies of the oscillation modes (e.g., Bischoff-Kim et al. 2019). The wandering of the frequencies takes place on timescales much longer than an observing season (roughly several months; Provencal et al. 2009), and the frequencies vary by much more than the measured asymmetries of ~ 1 μ Hz shown in Figure 6. Both time-varying dynamo magnetic fields (Markiel et al. 1994) and convective zone thicknesses (Montgomery et al. 2010, 2020) have been proposed for this phenomenon, although a definitive explanation remains elusive.

Curiously, most of GD 358’s asymmetries in Figure 6 lie in the magnetically forbidden region. The degree of asymmetry is too large to be explained by second-order rotational effects (Dziembowski & Goode 1992), which predict $\Delta_{-10+1}^{\ell=1} = P/20P_{\text{rot}}^2 \lesssim 10^{-2}$ μ Hz (the dashed purple curve in Figure 5), much lower than the observed values $\Delta_{-10+1}^{\ell=1} \sim 0.5$ μ Hz. If the asymmetries are magnetic in origin, ν_B^ℓ must be overestimated by a factor of $\gtrsim 6$. It is plausible that order-unity uncertainties in Equation 1 (for $B_{r,\text{crit}}$) and $a_{-10+1}^{\ell=1}$ may account for this. However, the measured asymmetries require very different field strengths for different radial orders. This suggests either that the magnetic field falls off quickly in the outer layers or that the asymmetries have a non-magnetic origin. In the latter case, the asymmetries may instead originate from GD 358’s drifting mode frequencies. This frequency wandering does not keep the asymmetry constant over time (cf. Figure 9 of Bischoff-Kim et al. 2019). We therefore suspect that the measured asymmetries result from wandering mode frequencies rather than magnetic shifts.

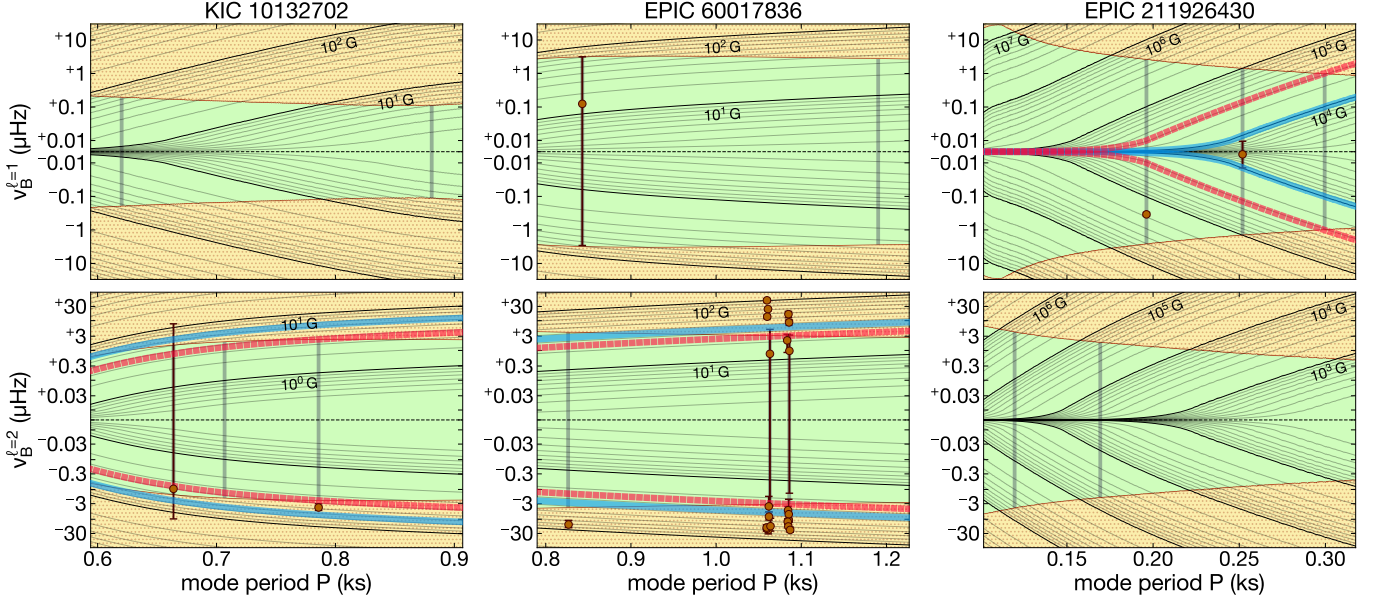


Figure 5. Leaf diagrams of three DAV WDs from [Hermes et al. \(2017a\)](#). *Brown circles* show measured asymmetry values, with error bars enclosing the 2σ confidence interval set by frequency measurement uncertainties. *Gray vertical lines* indicate an estimate for the central frequency of a multiplet. *Contours* indicate the degree of asymmetry implied by a given magnetic field. The *yellow dotted region* indicates the forbidden region within which magnetic mode suppression is expected. The *blue solid* contour indicates $B_{r,\text{shift}}$: this is the lowest-field strength contour that fully encloses a single *brown circle*, including its error bar. The *red dashed* contour indicates $B_{r,\text{supp}}$: this denotes the lowest-field strength contour that crosses all *gray vertical lines* outside of the *yellow dotted region*.

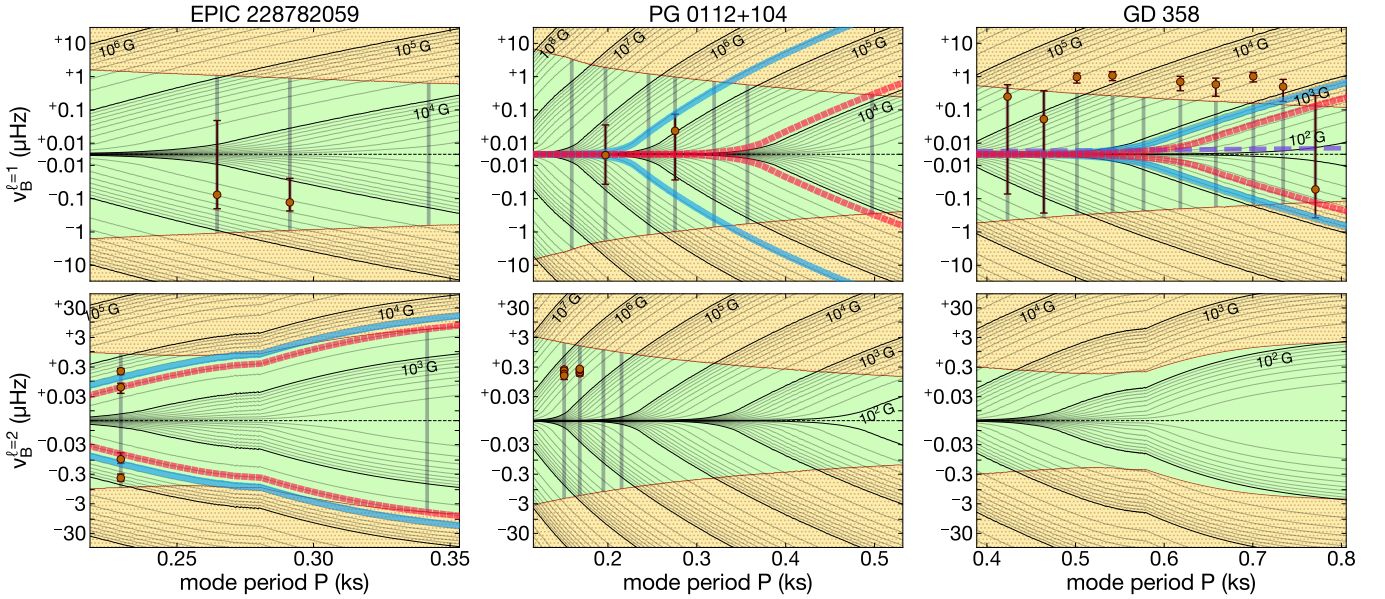


Figure 6. Same as Figure 6, but for the DBV WDs EPIC 228782059 ([Duan et al. 2021](#)), PG 0112+104 ([Hermes et al. 2017a](#)), and GD 358 ([Winget et al. 1994](#)). The *dashed purple curve* shows the predicted dipole asymmetry from second-order rotational effects.

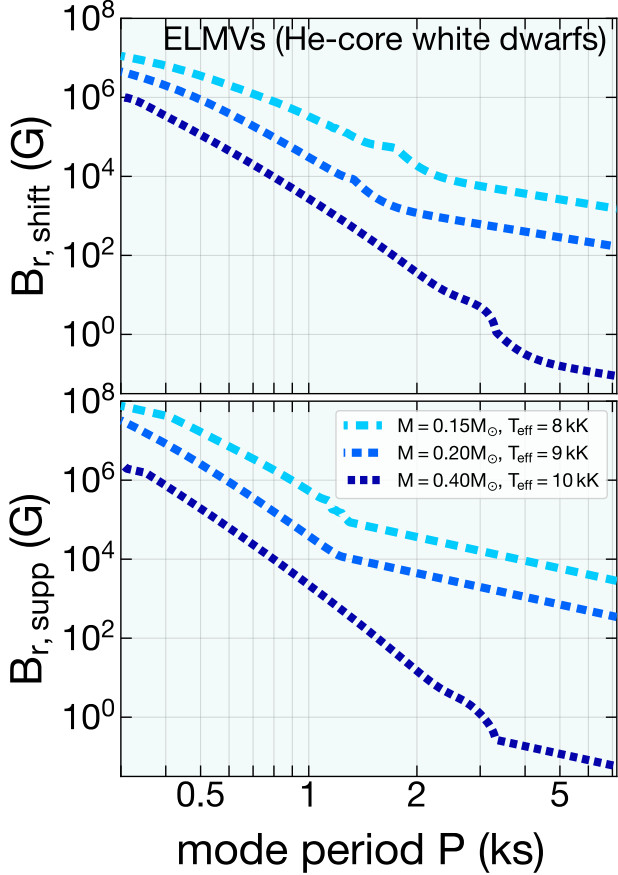


Figure 7. Model seismic magnetic field sensitivities $B_{r,\text{shift}}$ and $B_{r,\text{supp}}$ for $0.15M_{\odot}$, $0.20M_{\odot}$, and $0.40M_{\odot}$ helium-core WD pulsators on the DAV instability strip. These curves have been calculated for $\ell = 1$ and $\nu_B^{\ell=1} = 0.1 \mu\text{Hz}$.

Bagnulo & Landstreet (2022) conduct a volume-limited spectropolarimetric survey of nearby WDs, finding a dearth of magnetic fields in young ($\lesssim 2$ Gyr), canonical-mass WDs down to their detection limit (a few kilogauss). These spectropolarimetric measurements are shown in Figure 4. The low ($\lesssim 10$ kG) magnetic field limits we place on most of our carbon–oxygen WDs are consistent with this finding. In many cases, our seismic limits appear to be much more constraining, entailing magnetic fields less than ~ 100 G in several WDs with long-period pulsation modes.

4.3. ELMVs: probing the stripped cores of red giants?

Unlike carbon–oxygen WDs, helium-core WDs are exclusively produced by binary stellar evolution. These low-mass ($M \lesssim 0.5M_{\odot}$) WDs are the leftover cores of red giants whose envelopes have been stripped by a companion or ejected during a common-envelope event. To date, roughly 20 helium-core WDs are known to pulsate (Hermes et al. 2012, 2013b,c; Kilic et al. 2015; Gianni-

nas et al. 2016; Bell et al. 2017, 2018; Kilic et al. 2018; Pelisoli et al. 2018, 2019; Wang et al. 2020). These “extremely low-mass variables,” or ELMVs, are all located on a low- $\log g$ extension of the DAV instability strip (Gianninas et al. 2015; Tremblay et al. 2015a). As the direct descendants of the same red giants for which seismic magnetometry is already possible, helium-core WDs likely inherit the field strengths of the cores of their progenitors. Figure 7 shows the magnetic fields to which helium-core WD pulsators are sensitive.

We place an upper bound on GD 278, a low-mass ($M \approx 0.19M_{\odot}$) WD which pulsates in low-frequency gravity modes ($P \simeq 2400\text{--}6700$ s; Lopez et al. 2021). Assuming the mode identifications determined by Calcaferro et al. (2023), we find that the magnetic field in GD 278 is no larger than $B_{r,\text{supp}} \sim 70$ G (Figure 8). This field is much lower than those inferred for dipole-suppressed red giants ($\approx 20\%$ of all red giants; Stello et al. 2016), and smaller than the field expected to be generated by a core convective dynamo on the main sequence (Cantiello et al. 2016).

GD 278’s asymmetries are often close to or within the forbidden region, i.e., within the *yellow dotted region* in Figure 8). As discussed for GD 358, a magnetic origin for these asymmetries may still be possible if some order-unity prefactors are misestimated. The relatively fast rotation period $P_{\text{rot}} \approx 10$ hr (Lopez et al. 2021) corresponds to $P/P_{\text{rot}} \sim 10\%$ for the observed modes, suggesting that second-order rotational effects may play a role (shown as the *dashed purple curves* in Figure 8). Second-order rotational effects are expected to produce asymmetries $\Delta_{-10+1}^{\ell=1} = P/20P_{\text{rot}}^2 \simeq 0.2 \mu\text{Hz}$ in the two complete observed triplets at $P \approx 4030$ s and $P \approx 4760$ s (Dziembowski & Goode 1992). The observed asymmetries ($\Delta_{-10+1}^{\ell=1} = (0.44 \pm 0.06) \mu\text{Hz}$ and $\Delta_{-10+1}^{\ell=1} = (0.07 \pm 0.07) \mu\text{Hz}$, respectively) are similar in scale to (though at significant tension with) those predicted by second-order rotational effects. Further, we find that observed asymmetries do not consistently match second-order rotational asymmetries in sign. We also curiously find that observed quadrupole asymmetries are often lower than the expected second-order asymmetries by factors $\sim 3\text{--}10$ relative to predicted values (Dziembowski & Goode 1992). The ultimate origin of asymmetries in GD 278 are puzzling.

It is possible that GD 278’s progenitor was a lower-mass ($M \lesssim 1.2M_{\odot}$) main-sequence star below the Kraft break. Such stars have radiative cores, and are thus not expected to generate strong fields during the main sequence. If this is the case, it suggests that, in the absence of a convective core, the core field of a main-sequence star can be extremely low. In a $1M_{\odot}$ MESA

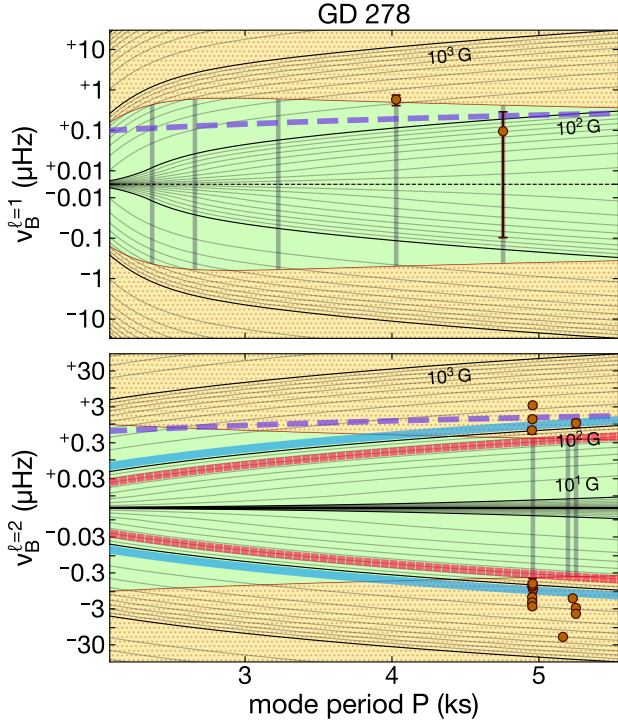


Figure 8. Same as Figure 5, but for the ELMV GD 278 (Lopez et al. 2021; Calcaferro et al. 2023). The *dashed purple curves* show the predicted asymmetries from second-order rotational effects on the dipole asymmetry $\Delta_{-10+1}^{\ell=2}$ and a typical quadrupole asymmetry $\Delta_{-10+2}^{\ell=2}$.

model, mass coordinates $\leq 0.19M_{\odot}$ are enclosed by a radius $R \approx 0.1R_{\odot}$ during the main-sequence. This decreases to $\approx 0.025R_{\odot}$ during the red giant branch, once the helium core has grown to $\approx 0.19R_{\odot}$. Assuming flux conservation, this implies that the core magnetic field of GD 278’s progenitor was no larger than $\simeq 4$ G on the main sequence. Alternatively, our upper bound may challenge the assumption of magnetic flux conservation between evolutionary stages.

At a time of rapid progress in red giant magnetoastroseismology, ELMVs may help test our understanding of magnetism in stellar cores as well as the essential pulsation physics itself. Since the near-surface WD fields to which seismology is sensitive can also be probed by spectroscopy or spectropolarimetry, comparison between the field strengths inferred by these techniques and seismology may serve as a valuable consistency check.

4.4. Caveats

The behavior of high-frequency pulsations under magnetic fields should be investigated in more detail. While we make a rudimentary correction for some non-asymptotic effects in this work, our correction leaves out some additional effects. Non-asymptotic modes may

produce significant displacements in evanescent regions, which are ignored by our integral estimate for \mathcal{I} in Equation 5. Further, as described in Appendix B, our results correct for non-asymptotic eigenfunctions in the calculation of \mathcal{I} . However, the derivation of Equation 4 (which writes ν_B^{ℓ} in terms of \mathcal{I}) still assumes certain terms scaling as $\sim 2\pi\nu/N$ are negligible, including effects of the horizontal field components and the radial displacement in the calculation of the mode inertia. Our estimates of magnetic effects also assume the mode wavelength is smaller than the scale height H on which quantities such as ρ and B change. For the long-period modes shown in Figure 2, the mode wavelengths are comparable to H just below the convective zone, making magnetic effects on modes more difficult to calculate. The effect of relaxing these assumptions should be investigated in more detail.

Our analysis also required basic assumptions about the dimensionless asymmetry parameters $a_{m_1 m_2 m_3}^{\ell}$, as well as the prefactor which appears in Equation 1 for $B_{r,\text{crit}}$. Both of these are order-unity functions of the field geometry (Lecoanet et al. 2017; Rui & Fuller 2023; Lecoanet et al. 2022) and sometimes the rotation rate, if it is high enough (Rui et al. 2024). This introduces an uncertain order-unity factor to our field estimates (e.g., Das et al. 2024). However, dipole/quadrupole asymmetries may fail more catastrophically when faced with, e.g., small-scale magnetic structures that cannot be resolved by $\ell = 1$ or $\ell = 2$ modes well enough to produce significant rotational multiplet asymmetries.

We also assume that the frequencies of each multiplet component have not been affected by nonlinear resonant mode coupling. However, WD pulsation modes occasionally show large, nonsecular frequency changes (e.g., Hermes et al. 2013a; Dalessio et al. 2013). In fact, some multiplet components within a pulsating WD have shown correlated, periodic frequency changes, a signature of resonant mode coupling (Zong et al. 2016). Such frequency changes could produce non-magnetic multiplet asymmetries.

Finally, this work stitches together a perturbative theory in $(B_r/B_{r,\text{crit}})^2$ for $B_r < B_{r,\text{crit}}$ with the assumption of total suppression when $B_r > B_{r,\text{crit}}$. In reality, perturbation theory is no longer valid once B_r is a large fraction of $B_{r,\text{crit}}$. Rui et al. (2024) show, for example, that the inappropriate application of perturbation theory overestimates the field strength in the case of a centered dipolar field aligned with the rotation axis. Along similar lines, strong-enough fields in slow-enough rotators are expected to align pulsations with the magnetic axis, dramatically increasing the complexity of a rotational multiplet in the power spectrum. These

strong magnetic effects should be more thoroughly investigated.

5. SUMMARY AND FUTURE DIRECTIONS

We summarize our conclusions in this work as follows:

1. WD pulsations can be used as a highly sensitive probe of the radial components of their near-surface magnetic fields. Magnetic fields are expected to asymmetricize rotational multiplets at intermediate field strengths $B_r \lesssim B_{r,\text{crit}}$ and suppress g-mode propagation when $B_r > B_{r,\text{crit}}$.
2. Seismology is most sensitive to magnetic fields in pulsating WDs with lower-frequency modes and thinner surface convection zones.
3. We place upper limits on the magnetic field in 20 DAV and 3 DBV carbon–oxygen WDs. Most upper limits in carbon–oxygen WDs lie within roughly $\sim 1\text{--}10$ kG, but they can be as low as a *few to tens of gauss* when low-frequency modes ($\gtrsim 800$ s) are not observed to be suppressed. Seismology may help uncover the as-of-yet unknown formation mechanism of strong magnetic fields in WDs at low effective temperatures.
4. We also place an upper limit on the near-surface magnetic field $\simeq 70$ G in the ELMV GD 278 (helium-core) WD. As stripped red giants, ELMVs may present a valuable opportunity to test our understanding of red giant magnetism as well as the fundamental pulsation physics.

Seismic WD magnetometry affords many further possibilities. Pulsating WDs are a highly diverse class which also include pre-WDs (GW Virs/DOVs/PNNVs, e.g., Winget et al. 1991; Sowicka et al. 2023), pre-ELMVs (e.g., Maxted et al. 2013), and pulsating accretors in cataclysmic variables (GW Lib, e.g., Van Zyl

et al. 2004). Additionally, several pulsating ultramassive ($M \gtrsim 1.1M_\odot$) DAV WDs are known (Hermes et al. 2013d; Curd et al. 2017; Kanaan et al. 2005; Rowan et al. 2019; Vincent et al. 2020; Kilic et al. 2023a) which, unlike the WDs considered in this work, have already begun to crystallize on the DAV instability strip. This is expected to affect their pulsations (Kanaan et al. 2005; Nitta et al. 2015; De Gerónimo et al. 2019), possibly allowing them to help uncover the relationship between their crystallization and magnetization. Finally, some hot subdwarfs are known to pulsate in gravity modes (Pablo et al. 2012; Telting et al. 2014; Baran et al. 2016, 2019; Silvotti et al. 2019; Sanjayan et al. 2022; Silvotti et al. 2022; Ma et al. 2023), which are likely sensitive to their near-core fields. Seismology may contribute to the solution of an open problem regarding the dearth of observed hot subdwarf magnetism (Dorsch et al. 2022; Pelisoli et al. 2022; Pakmor et al. 2024; Dorsch et al. 2024).

We thank Sivan Ginzburg for helpful discussions and comments on the manuscript. We are grateful for support from the United States–Israel Binational Science Foundation through grant BSF-2022175. N.Z.R. acknowledges support from the National Science Foundation Graduate Research Fellowship under Grant No. DGE-1745301.

Facilities: None

Software: MESA (Paxton et al. 2010, 2013, 2015, 2018), NumPy (Oliphant et al. 2006), SciPy (Virtanen et al. 2020), AstroPy (Robitaille et al. 2013), Matplotlib (Hunter 2007; Team 2024)

REFERENCES

- Aerts, C. 2021, *Reviews of Modern Physics*, 93, 015001
- Aerts, C., Christensen-Dalsgaard, J., & Kurtz, D. W. 2010, *Asteroseismology* (Springer Science & Business Media)
- Bagnulo, S., & Landstreet, J. 2021, *Monthly Notices of the Royal Astronomical Society*, 507, 5902
- Bagnulo, S., & Landstreet, J. D. 2022, *The Astrophysical Journal Letters*, 935, L12
- Baran, A., Telting, J., Németh, P., et al. 2016, *Astronomy & Astrophysics*, 585, A66
- Baran, A. S., Telting, J., Jeffery, C. S., et al. 2019, *Monthly Notices of the Royal Astronomical Society*, 489, 1556
- Bédard, A., Bergeron, P., Brassard, P., & Fontaine, G. 2020, *The Astrophysical Journal*, 901, 93
- Bell, K. J., Gianninas, A., Hermes, J., et al. 2017, *The Astrophysical Journal*, 835, 180
- Bell, K. J., Pelisoli, I., Kepler, S. O., et al. 2018, *Astronomy & Astrophysics*, 617, A6
- Bischoff-Kim, A., Provencal, J., Bradley, P. A., et al. 2019, *The Astrophysical Journal*, 871, 13

- Blatman, D., & Ginzburg, S. 2024a, *Monthly Notices of the Royal Astronomical Society*, 528, 3153
- . 2024b, *Monthly Notices of the Royal Astronomical Society: Letters*, slae054
- Brassard, P., Fontaine, G., Wesemael, F., & Hansen, C. 1992, *Astrophysical Journal Supplement Series* (ISSN 0067-0049), vol. 80, no. 1, May 1992, p. 369-401. Research supported by NSERC and Ministère de l'Éducation du Québec., 80, 369
- Brickhill, A. 1991, *Monthly Notices of the Royal Astronomical Society*, 251, 673
- Briggs, G. P., Ferrario, L., Tout, C. A., & Wickramasinghe, D. T. 2018, *Monthly Notices of the Royal Astronomical Society*, 478, 899
- Bugnet, L., Prat, V., Mathis, S., et al. 2021, *Astronomy & Astrophysics*, 650, A53
- Calcaferro, L. M., Córscico, A. H., Althaus, L. G., Lopez, I. D., & Hermes, J. 2023, *Astronomy & Astrophysics*, 673, A135
- Cantiello, M., Fuller, J., & Bildsten, L. 2016, *The Astrophysical Journal*, 824, 14
- Córscico, A. H., Althaus, L. G., Miller Bertolami, M. M., & Kepler, S. O. 2019, *The Astronomy and Astrophysics Review*, 27, 7
- Curd, B., Gianninas, A., Bell, K. J., et al. 2017, *Monthly Notices of the Royal Astronomical Society*, 468, 239
- Dalessio, J., Sullivan, D., Provencal, J., et al. 2013, *The Astrophysical Journal*, 765, 5
- Das, S. B., Einramhof, L., & Bugnet, L. 2024, arXiv preprint arXiv:2405.20133
- De Gerónimo, F. C., Córscico, A. H., Althaus, L. G., Wachlin, F. C., & Camisassa, M. E. 2019, *Astronomy & Astrophysics*, 621, A100
- Deheuvels, S., Li, G., Ballot, J., & Lignières, F. 2023, *Astronomy & Astrophysics*, 670, L16
- Deheuvels, S., Ouazzani, R.-M., & Basu, S. 2017, *Astronomy & Astrophysics*, 605, A75
- Dolez, N., Vauclair, G., Kleinman, S. J., et al. 2006, *Astronomy & Astrophysics*, 446, 237
- Dorsch, M., Reindl, N., Pelisoli, I., et al. 2022, *Astronomy & Astrophysics*, 658, L9
- Dorsch, M., Jeffery, C., Monai, A. P., et al. 2024, arXiv preprint arXiv:2410.02737
- Duan, R., Zong, W., Fu, J.-N., et al. 2021, *The Astrophysical Journal*, 922, 2
- Dufour, P., Fontaine, G., Liebert, J., Williams, K., & Lai, D. K. 2008, *The Astrophysical Journal*, 683, L167
- Dufour, P., Desharnais, S., Wesemael, F., et al. 2010, *The Astrophysical Journal*, 718, 647
- Dziembowski, W., & Goode, P. R. 1992, *Astrophysical Journal*, Part 1 (ISSN 0004-637X), vol. 394, no. 2, Aug. 1, 1992, p. 670-687. Research supported by NSF and SERC., 394, 670
- Ferrario, L., de Martino, D., & Gänsicke, B. T. 2015, *Space Science Reviews*, 191, 111
- Fontaine, G., & Wesemael, F. 1987, in *IAU Colloq. 95: Second Conference on Faint Blue Stars*, 319–326
- Fu, J.-N., Vauclair, G., Solheim, J.-E., et al. 2007, *Astronomy & Astrophysics*, 467, 237
- Fuentes, J., Castro-Tapia, M., & Cumming, A. 2024, arXiv preprint arXiv:2402.03639
- Fuller, J., Cantiello, M., Stello, D., Garcia, R. A., & Bildsten, L. 2015, *Science*, 350, 423
- García, R., Hernández, F. P., Benomar, O., et al. 2014, *Astronomy & Astrophysics*, 563, A84
- García-Berro, E., Lorén-Aguilar, P., Aznar-Siguán, G., et al. 2012, *The Astrophysical Journal*, 749, 25
- Gentile Fusillo, N., Tremblay, P.-E., Cukanovaite, E., et al. 2021, *Monthly Notices of the Royal Astronomical Society*, 508, 3877
- Gianninas, A., Curd, B., Fontaine, G., Brown, W. R., & Kilic, M. 2016, *The Astrophysical Journal Letters*, 822, L27
- Gianninas, A., Kilic, M., Brown, W. R., Canton, P., & Kenyon, S. J. 2015, *The Astrophysical Journal*, 812, 167
- Ginzburg, S., Fuller, J., Kawka, A., & Caiazzo, I. 2022, *Monthly Notices of the Royal Astronomical Society*, 514, 4111
- Gizon, L., & Solanki, S. 2003, *The Astrophysical Journal*, 589, 1009
- Goldreich, P., & Wu, Y. 1999, *The Astrophysical Journal*, 511, 904
- Hatt, E. J., Ong, J. J., Nielsen, M. B., et al. 2024, *Monthly Notices of the Royal Astronomical Society*, 534, 1060
- Hermes, J., Kawaler, S. D., Bischoff-Kim, A., et al. 2017a, *The Astrophysical Journal*, 835, 277
- Hermes, J., Montgomery, M., Winget, D., et al. 2012, *The Astrophysical Journal Letters*, 750, L28
- Hermes, J., Montgomery, M. H., Mullally, F., Winget, D., & Bischoff-Kim, A. 2013a, *The Astrophysical Journal*, 766, 42
- Hermes, J., Montgomery, M. H., Winget, D., et al. 2013b, *The Astrophysical Journal*, 765, 102
- Hermes, J., Montgomery, M. H., Gianninas, A., et al. 2013c, *Monthly Notices of the Royal Astronomical Society*, 436, 3573
- Hermes, J., Gänsicke, B., Bischoff-Kim, A., et al. 2015, *Monthly Notices of the Royal Astronomical Society*, 451, 1701

- Hermes, J., Gänsicke, B. T., Kawaler, S. D., et al. 2017b, *The Astrophysical Journal Supplement Series*, 232, 23
- Hermes, J. J., Kepler, S. O., Castanheira, B. G., et al. 2013d, *The Astrophysical Journal Letters*, 771, L2
- Hunter, J. D. 2007, *Computing in Science & Engineering*, 9, 90, doi: [10.1109/MCSE.2007.55](https://doi.org/10.1109/MCSE.2007.55)
- Isern, J., García-Berro, E., Külebi, B., & Lorén-Aguilar, P. 2017, *The Astrophysical Journal Letters*, 836, L28
- Jones, P. W., Pesnell, W. D., Hansen, C. J., & Kawaler, S. D. 1989, *Astrophysical Journal*, Part 1 (ISSN 0004-637X), vol. 336, Jan. 1, 1989, p. 403-408., 336, 403
- Kanaan, A., Nitta, A., Winget, D. E., et al. 2005, *Astronomy & Astrophysics*, 432, 219
- Kawaler, S. D., O'Brien, M. S., Clemens, J. C., et al. 1995, *The astrophysical journal*. Chicago. Vol. 450, no. 1, pt. 1 (Sept. 1995), p. 350-363
- Kilic, M., Córscico, A. H., Moss, A. G., et al. 2023a, *Monthly Notices of the Royal Astronomical Society*, 522, 2181
- Kilic, M., Hermes, J., Gianninas, A., & Brown, W. R. 2015, *Monthly Notices of the Royal Astronomical Society: Letters*, 446, L26
- Kilic, M., Hermes, J., Corsico, A. H., et al. 2018, *Monthly Notices of the Royal Astronomical Society*, 479, 1267
- Kilic, M., Moss, A. G., Kosakowski, A., et al. 2023b, *Monthly Notices of the Royal Astronomical Society*, 518, 2341
- Landstreet, J. D. 2014, *Proceedings of the International Astronomical Union*, 9, 311
- Lecoanet, D., Bowman, D. M., & Van Reeth, T. 2022, *Monthly Notices of the Royal Astronomical Society: Letters*, 512, L16
- Lecoanet, D., Vasil, G. M., Fuller, J., Cantiello, M., & Burns, K. J. 2017, *Monthly Notices of the Royal Astronomical Society*, 466, 2181
- Ledoux, P. 1951, *Astrophysical Journal*, 114
- Li, G., Deheuvels, S., Ballot, J., & Lignières, F. 2022, *Nature*, 610, 43
- Li, G., Deheuvels, S., Li, T., Ballot, J., & Lignières, F. 2023, *Astronomy & Astrophysics*, 680, A26
- Loi, S. T. 2020, *Monthly Notices of the Royal Astronomical Society*, 496, 3829
- Loi, S. T., & Papaloizou, J. C. 2017, *Monthly Notices of the Royal Astronomical Society*, 467, 3212
- . 2018, *Monthly Notices of the Royal Astronomical Society*, 477, 5338
- Lopez, I. D., Hermes, J., Calcaferro, L. M., et al. 2021, *The Astrophysical Journal*, 922, 220
- Ma, X.-Y., Zong, W., Fu, J.-N., et al. 2023, *Astronomy & Astrophysics*, 680, A11
- Markiel, J. A., Thomas, J. H., & Van Horn, H. 1994, *The Astrophysical Journal*, vol. 430, no. 2, pt. 1, p. 834-838, 430, 834
- Mathis, S., & Bugnet, L. 2023, arXiv preprint arXiv:2306.11587
- Maxted, P. F., Serenelli, A. M., Miglio, A., et al. 2013, *Nature*, 498, 463
- Montgomery, M. H., Hermes, J., Winget, D. E., Dunlap, B. H., & Bell, K. J. 2020, *The Astrophysical Journal*, 890, 11
- Montgomery, M. H., Provencal, J. L., Kanaan, A., et al. 2010, *The Astrophysical Journal*, 716, 84
- Mosser, B., Belkacem, K., Pinçon, C., et al. 2017, *Astronomy & Astrophysics*, 598, A62
- Nitta, A., Kepler, S., Chené, A.-N., et al. 2015, *Proceedings of the International Astronomical Union*, 11, 493
- Oliphant, T. E., et al. 2006, *Guide to numpy*, Vol. 1 (Trelgol Publishing USA)
- Ong, J. J., Bugnet, L., & Basu, S. 2022, *The Astrophysical Journal*, 940, 18
- Pablo, H., Kawaler, S. D., Reed, M. D., et al. 2012, *Monthly Notices of the Royal Astronomical Society*, 422, 1343
- Pakmor, R., Pelisoli, I., Justham, S., et al. 2024
- Paxton, B., Bildsten, L., Dotter, A., et al. 2010, *The Astrophysical Journal Supplement Series*, 192, 3
- Paxton, B., Cantiello, M., Arras, P., et al. 2013, *The Astrophysical Journal Supplement Series*, 208, 4
- Paxton, B., Marchant, P., Schwab, J., et al. 2015, *The Astrophysical Journal Supplement Series*, 220, 15
- Paxton, B., Schwab, J., Bauer, E. B., et al. 2018, *The Astrophysical Journal Supplement Series*, 234
- Pelisoli, I., Bell, K. J., Kepler, S. O., & Koester, D. 2019, *Monthly Notices of the Royal Astronomical Society*, 482, 3831
- Pelisoli, I., Kepler, S. O., Koester, D., et al. 2018, *Monthly Notices of the Royal Astronomical Society*, 478, 867
- Pelisoli, I., Dorsch, M., Heber, U., et al. 2022, *Monthly Notices of the Royal Astronomical Society*, 515, 2496
- Pinçon, C., & Takata, M. 2022, *Astronomy & Astrophysics*, 661, A139
- Provencal, J. L., Montgomery, M. H., Kanaan, A., et al. 2009, *The Astrophysical Journal*, 693, 564
- Robitaille, T. P., Tollerud, E. J., Greenfield, P., et al. 2013, *Astronomy & Astrophysics*, 558, A33
- Rowan, D. M., Tucker, M. A., Shappee, B. J., & Hermes, J. J. 2019, *Monthly Notices of the Royal Astronomical Society*, 486, 4574
- Rui, N. Z., & Fuller, J. 2023, *Monthly Notices of the Royal Astronomical Society*, 523, 582

- Rui, N. Z., Ong, J. J., & Mathis, S. 2024, *Monthly Notices of the Royal Astronomical Society*, 527, 6346
- Sanjayan, S., Baran, A., Ostrowski, J., et al. 2022, *Monthly Notices of the Royal Astronomical Society*, 509, 763
- Schmidt, G. D., & Grauer, A. D. 1997, *The Astrophysical Journal*, 488, 827
- Schneider, F., Ohlmann, S., Podsiadlowski, P., et al. 2020, *Monthly Notices of the Royal Astronomical Society*, 495, 2796
- Schreiber, M. R., Belloni, D., Gänsicke, B. T., Parsons, S. G., & Zorotovic, M. 2021, *Nature Astronomy*, 5, 648
- Silvotti, R., Németh, P., Telting, J. H., et al. 2022, *Monthly Notices of the Royal Astronomical Society*, 511, 2201
- Silvotti, R., Uzundag, M., Baran, A., et al. 2019, *Monthly Notices of the Royal Astronomical Society*, 489, 4791
- Sowicka, P., Handler, G., Jones, D., et al. 2023, *The Astrophysical Journal Supplement Series*, 269, 32
- Stello, D., Cantiello, M., Fuller, J., et al. 2016, *Nature*, 529, 364
- Team, T. M. D. 2024, *Matplotlib: Visualization with Python, v3.9.2*, Zenodo, doi: [10.5281/zenodo.13308876](https://doi.org/10.5281/zenodo.13308876)
- Telting, J., Östensen, R., Reed, M., et al. 2014, in *6th Meeting on Hot Subdwarf Stars and Related Objects*, Vol. 481, 287
- Tout, C. A., Wickramasinghe, D., Liebert, J., Ferrario, L., & Pringle, J. 2008, *Monthly Notices of the Royal Astronomical Society*, 387, 897
- Townsend, R., & Teitler, S. 2013, *Monthly Notices of the Royal Astronomical Society*, 435, 3406
- Tremblay, P.-E., Gianninas, A., Kilic, M., et al. 2015a, *The Astrophysical Journal*, 809, 148
- Tremblay, P.-E., Ludwig, H.-G., Freytag, B., et al. 2015b, *The Astrophysical Journal*, 799, 142
- Unno, W., Osaki, Y., Ando, H., & Shibahashi, H. 1979, Tokyo: University of Tokyo Press
- Van Grootel, V., Fontaine, G., Brassard, P., & Dupret, M.-A. 2012, *The Astrophysical Journal*, 762, 57
- Van Zyl, L., Warner, B., O'Donoghue, D., et al. 2004, *Monthly Notices of the Royal Astronomical Society*, 350, 307
- Vauclair, G., Moskalik, P., Pfeiffer, B., et al. 2002, *Astronomy & Astrophysics*, 381, 122
- Vincent, O., Bergeron, P., & Lafrenière, D. 2020, *The Astronomical Journal*, 160, 252
- Virtanen, P., Gommers, R., Oliphant, T. E., et al. 2020, *Nature methods*, 17, 261
- Wang, K., Zhang, X., & Dai, M. 2020, *The Astrophysical Journal*, 888, 49
- Williams, K. A., Montgomery, M., Winget, D., Falcon, R. E., & Bierwagen, M. 2016, *The Astrophysical Journal*, 817, 27
- Winget, D. E., Hansen, C. J., Fontaine, G., et al. 1991, *The astrophysical journal. Chicago*. Vol. 378, no. 1, pt. 1 (Sept. 1991), p. 326-346
- Winget, D. E., Nather, R. E., Clemens, J. C., et al. 1994, *The astrophysical journal. Chicago*. Vol. 430, no. 2, pt. 1 (Aug. 1994), p. 839-849
- Zong, W., Charpinet, S., Vauclair, G., Giammichele, N., & Van Grootel, V. 2016, *Astronomy & Astrophysics*, 585, A22

APPENDIX

A. MAGNETIC FORMALISM

The asymmetry-based magnetic field bounds placed in this work require concrete assumptions about the asymmetry parameters $a_{m_1 m_2 m_3}^\ell$. This Appendix derives the dipole and quadrupole asymmetry parameters assumed in this study.

A.1. *Magnetic frequency shifts of g-mode pulsations*

In the most common formalism (Bugnet et al. 2021; Li et al. 2022; Das et al. 2024), the Coriolis and Lorentz forces are assumed to be weak and degenerate perturbation theory is applied. The incompressible and asymptotic approximations (appropriate for high-radial order g modes) are additionally assumed. Furthermore, it is assumed either that the magnetic field is axisymmetric about the rotation axis or that the effect of the Coriolis force on the waves is much stronger than that of the Lorentz force. In both cases, the eigenfunctions are aligned with the rotation axis, and the frequency shifts are only sensitive to azimuthal averages of B_r^2 , i.e.,

$$\langle B_r^2 \rangle_\phi = \int_0^{2\pi} \frac{d\phi}{2\pi} B_r^2, \quad (\text{A1})$$

although the field's dependence on the colatitude $\mu = \cos \theta$ still matters.

In the inertial frame, the frequency shifts $\delta\nu$ of the dipole modes are given by Equations 32 and 33 of Li et al. (2022):

$$\delta\nu_{m=0}^{\ell=1} = \mathcal{B}^{\ell=1} \left[\frac{3}{2}(1 - \mu^2) \right] \quad (\text{A2a})$$

$$\delta\nu_{m=\pm 1}^{\ell=1} = \pm \frac{1}{2} \frac{\langle \Omega \rangle_g}{2\pi} + \mathcal{B}^{\ell=1} \left[\frac{3}{4}(1 + \mu^2) \right], \quad (\text{A2b})$$

and the same for the quadrupole modes are given by Appendix C.1 of Das et al. (2024):

$$\delta\nu_{m=0}^{\ell=2} = \mathcal{B}^{\ell=2} \left[\frac{15}{2}(\mu^2 - \mu^4) \right] \quad (\text{A3a})$$

$$\delta\nu_{m=\pm 1}^{\ell=2} = \pm \frac{5}{6} \frac{\langle \Omega \rangle_g}{2\pi} + \mathcal{B}^{\ell=2} \left[\frac{5}{4}(1 - 3\mu^2 + 4\mu^4) \right] \quad (\text{A3b})$$

$$\delta\nu_{m=\pm 2}^{\ell=2} = \pm \frac{5}{3} \frac{\langle \Omega \rangle_g}{2\pi} + \mathcal{B}^{\ell=2} \left[\frac{5}{4}(1 - \mu^4) \right], \quad (\text{A3c})$$

where the relevant integral average operation $\mathcal{B}^\ell[\cdot]$ is given under the present assumptions by

$$\mathcal{B}^\ell[f(\mu)] \approx \nu_B^\ell \int_{\mathcal{R}_\nu^\ell} dr K(r) \int_{S^2} \frac{d\Omega}{4\pi} B_r^2 f(\mu). \quad (\text{A4})$$

If the Lorentz force is instead comparable to or stronger than the Coriolis force, the frequency shifts it causes are still at the same order of magnitude as ν_B^ℓ (as in Equation 4), although the dimensionless prefactors are given by the solution of a more complicated matrix problem, and multiplets generally possess more than $2\ell + 1$ peaks in the inertial frame (see the discussion in the Supplementary Information of Li et al. 2022). This does not seem to be the case in any of the WDs we analyze, since all of their (possibly incomplete) rotational multiplets are broadly recognizable and lack significant extra frequency peaks.

A.2. *Multiplet asymmetries due to magnetism*

When $K(r)$ is sharply peaked and the magnetic frequency shifts are only sensitive to a geometrically thin radial shell (which is often true, especially in the WD case), the radial integral in Equation A4 becomes independent of the angular one, and we can speak of a single horizontal dependence of B_r . In other words, we can approximately take

$$B_r(r, \mu, \phi) = A(r) \psi(\mu, \phi), \quad (\text{A5})$$

where we normalize the horizontal dependence of B_r to $\psi = \psi(\mu, \phi)$ such that $\int_{S^2} \psi^2 \sin \theta \, d\theta \, d\phi = 1$. We define the azimuthal average $\langle \psi^2 \rangle_\phi$ as

$$\langle \psi^2 \rangle_\phi \equiv \int_0^{2\pi} \frac{d\phi}{2\pi} \psi^2. \quad (\text{A6})$$

Under this condition, [Li et al. \(2022\)](#) show that the dipole asymmetry parameter is given by

$$a_{-10+1}^{\ell=1} = \int_{-1}^{+1} \langle \psi^2 \rangle_\phi \frac{1}{2} (3\mu^2 - 1) \, d\mu, \quad (\text{A7})$$

and encodes some information about the geometry of the field.

We generalize the parameter $a_{-10+1}^{\ell=1}$ to describe the asymmetry between any three modes within the same multiplet, including those involving higher-degree ($\ell > 1$) modes such as quadrupole modes ($\ell = 2$). We start by noticing that the linear combination of frequencies in Equation 9 is useful because it depends on neither the unperturbed frequencies $\nu^{(0)}$ (which are the same for all modes within a multiplet) nor the rotational splitting (which is proportional to m). In other words, for three modes with equal k and ℓ but distinct azimuthal orders m_1 , m_2 , and m_3 , maximally “useful” linear combinations $\Delta_{m_1 m_2 m_3}^\ell$ of measured frequencies of the form

$$\Delta_{m_1 m_2 m_3}^\ell = c_1 \nu_{m_1}^\ell + c_2 \nu_{m_2}^\ell + c_3 \nu_{m_3}^\ell. \quad (\text{A8})$$

should satisfy $c_1 + c_2 + c_3 = 0$ and $m_1 c_1 + m_2 c_2 + m_3 c_3 = 0$ to cancel out $\nu^{(0)}$ and $\langle \Omega \rangle_g$, respectively.

For concreteness, for the quadrupole modes, we choose the coefficients c_1 , c_2 , and c_3 to be small integers. There are $2\ell+1 C_3 = 10$ distinct useful linear combinations:

$$\Delta_{-2-10}^{\ell=2} = \nu_{m=-2}^{\ell=2} - 2\nu_{m=-1}^{\ell=2} + \nu_{m=0}^{\ell=2} \quad (\text{A9a})$$

$$\Delta_{-2-1+1}^{\ell=2} = 2\nu_{m=-2}^{\ell=2} - 3\nu_{m=-1}^{\ell=2} + \nu_{m=+1}^{\ell=2} \quad (\text{A9b})$$

$$\Delta_{-2-1+2}^{\ell=2} = 3\nu_{m=-2}^{\ell=2} - 4\nu_{m=-1}^{\ell=2} + \nu_{m=+2}^{\ell=2} \quad (\text{A9c})$$

$$\Delta_{-20+1}^{\ell=2} = \nu_{m=-2}^{\ell=2} - 3\nu_{m=0}^{\ell=2} + 2\nu_{m=+1}^{\ell=2} \quad (\text{A9d})$$

$$\Delta_{-20+2}^{\ell=2} = \nu_{m=-2}^{\ell=2} - 2\nu_{m=0}^{\ell=2} + \nu_{m=+2}^{\ell=2} \quad (\text{A9e})$$

$$\Delta_{-2+1+2}^{\ell=2} = \nu_{m=-2}^{\ell=2} - 4\nu_{m=+1}^{\ell=2} + 3\nu_{m=+2}^{\ell=2} \quad (\text{A9f})$$

$$\Delta_{-10+1}^{\ell=2} = \nu_{m=-1}^{\ell=2} - 2\nu_{m=0}^{\ell=2} + \nu_{m=+1}^{\ell=2} \quad (\text{A9g})$$

$$\Delta_{-10+2}^{\ell=2} = 2\nu_{m=-1}^{\ell=2} - 3\nu_{m=0}^{\ell=2} + \nu_{m=+2}^{\ell=2} \quad (\text{A9h})$$

$$\Delta_{-1+1+2}^{\ell=2} = \nu_{m=-1}^{\ell=2} - 3\nu_{m=+1}^{\ell=2} + 2\nu_{m=+2}^{\ell=2} \quad (\text{A9i})$$

$$\Delta_{0+1+2}^{\ell=2} = \nu_{m=0}^{\ell=2} - 2\nu_{m=+1}^{\ell=2} + \nu_{m=+2}^{\ell=2}, \quad (\text{A9j})$$

Although only $2\ell - 1 = 3$ of these contain independent information, observed multiplets are often incomplete, restricting which of these 10 asymmetry parameters can be calculated. In general, whether a given mode is observable depends on the excitation mechanism as well as viewing angle (see [Gizon & Solanki 2003](#) and [Das et al. 2024](#) for further discussion). WD modes are also not generally in energy equipartition, and even modes within the same multiplet can be excited to very different amplitudes ([Hermes et al. 2015](#)).

Following the normalization convention of [Li et al. \(2022\)](#) and [Das et al. \(2024\)](#), these linear combinations are related to dimensionless asymmetry parameters $a_{m_1 m_2 m_3}^\ell$ using Equations 8 and 10. Using Equation A6, we rewrite the operator $\mathcal{B}^\ell[\cdot]$ as

$$\mathcal{B}^\ell[f(\mu)] \approx \nu_B^\ell \int_{-1}^{+1} \langle \psi^2 \rangle_\phi f(\mu) \, d\mu. \quad (\text{A10})$$

Equations A3 for the quadrupole frequency shifts then imply that

$$\begin{aligned}
a_{-2-10}^{\ell=2} &= a_{0+1+2}^{\ell=2} \\
&= \int_{-1}^{+1} \langle \psi^2 \rangle_\phi \frac{1}{4} (-15\mu^4 + 12\mu^2 - 1) d\mu
\end{aligned} \tag{A11a}$$

$$\begin{aligned}
a_{-2-1+1}^{\ell=2} &= a_{-2-1+2}^{\ell=2} = a_{-2+1+2}^{\ell=2} = a_{-1+1+2}^{\ell=2} \\
&= \int_{-1}^{+1} \langle \psi^2 \rangle_\phi \frac{1}{2} (-5\mu^4 + 3\mu^2) d\mu
\end{aligned} \tag{A11b}$$

$$\begin{aligned}
a_{-20+1}^{\ell=2} &= a_{-10+2}^{\ell=2} \\
&= \int_{-1}^{+1} \langle \psi^2 \rangle_\phi \frac{1}{4} (25\mu^4 - 24\mu^2 + 3) d\mu
\end{aligned} \tag{A11c}$$

$$a_{-20+2}^{\ell=2} = \int_{-1}^{+1} \langle \psi^2 \rangle_\phi \frac{1}{2} (5\mu^4 - 6\mu^2 + 1) d\mu \tag{A11d}$$

$$a_{-10+1}^{\ell=2} = \int_{-1}^{+1} \langle \psi^2 \rangle_\phi \frac{1}{2} (10\mu^4 - 9\mu^2 + 1) d\mu. \tag{A11e}$$

Curiously, five groups of dimensionless asymmetry parameters in Equations A11 are constrained to be equal. This is not a field geometry-dependent fact, but rather a result of the assumption that rotation fixes the preferred direction respected by the modes. It is also distinct from the linear dependence of the linear combinations of frequencies in Equations A9, although they are self-consistent. For example, Equations A9 and 10 easily show that $\Delta_{-10+1}^{\ell=2} + 2\Delta_{0+1+2}^{\ell=2} = \Delta_{-1+1+2}^{\ell=2}$, a relationship which is obeyed by the expressions in Equations A11.

On the one hand, this implies that not all of the modes in a quintuplet are required to be measured to extract all of the information the quintuplet encodes. Conversely, checking that these linear combinations of quadrupole modes in fact obey these relationships may be a useful test in determining whether observed asymmetries are in fact magnetic in origin (under the present assumptions).

A.3. Asymmetry parameters for an inclined dipole

For a centered dipole magnetic field with some obliquity angle β relative to the rotation axis, the normalized horizontal dependence of B_r is given by

$$\psi(\mu, \phi) = \frac{1}{2} \sqrt{\frac{3}{\pi}} (\cos \beta \cos \theta + \sin \beta \sin \theta \cos \phi), \tag{A12}$$

cf. Mathis & Bugnet (2023) and Das et al. (2024).

Averaging ψ^2 over ϕ gives

$$\langle \psi^2 \rangle_\phi = \frac{3}{2} P_2(\cos \beta) \mu^2 + \frac{3}{4} \sin^2 \beta \tag{A13}$$

where $P_2(x) = (3x^2 - 1)/2$ is a Legendre polynomial.

The form of Equation A13 is highly instructive. It writes $\langle \psi^2 \rangle_\phi$ as two terms, the second of which is a constant over the star and therefore shifts all modes equally (i.e., cannot introduce asymmetries). Since all asymmetry parameters only depend on the field through latitudinal averages over $\langle \psi^2 \rangle_\phi$, every asymmetry parameter defined in Equations A7 and A11 must be proportional to $P_2(\cos \beta)$ (and therefore to each other, in ratios which are independent of β). Moreover, all asymmetry parameters of any ℓ (including $\ell > 2$) must vanish for all β at some critical obliquity $\beta = \arccos(-1/3)/2$ where $P_2(\cos \beta)$ vanishes (this has been noticed in special cases by Mathis & Bugnet 2023 and Das et al. 2024). This appears to be a special property of the dipole geometry, where the relevant component of $\langle \psi^2 \rangle_\phi$ depends on β and μ only in a “disentangled” way.

Evaluating Equations A7 and A11, we have

$$a_{-10+1}^{\ell=1} = \frac{2}{5} P_2(\cos \beta) \tag{A14}$$

for $\ell = 1$, and

$$a_{-2-10}^{\ell=2} = a_{-10+1}^{\ell=2} = a_{0+1+2}^{\ell=2} = -\frac{2}{35}P_2(\cos\beta) \quad (\text{A15a})$$

$$a_{-2-1+1}^{\ell=2} = a_{-20+1}^{\ell=2} = a_{-10+2}^{\ell=2} = a_{-1+1+2}^{\ell=2} = -\frac{6}{35}P_2(\cos\beta) \quad (\text{A15b})$$

$$a_{-2-1+2}^{\ell=2} = a_{-2+1+2}^{\ell=2} = -\frac{12}{35}P_2(\cos\beta) \quad (\text{A15c})$$

$$a_{-20+2}^{\ell=2} = -\frac{8}{35}P_2(\cos\beta) \quad (\text{A15d})$$

for $\ell = 2$.

If all possible magnetic axes are equally probable, $P_2(\cos\beta)$ has a root-mean-square value

$$\begin{aligned} P_2(\cos\beta)_{\text{rms}} &= \sqrt{\frac{1}{2} \int_{-1}^{+1} P_2(\cos\beta)^2 d(\cos\beta)} \\ &= \sqrt{\frac{2}{5}} \approx 0.63 \end{aligned} \quad (\text{A16})$$

We adopt this root-mean-square value as the fiducial value of $P_2(\cos\beta)$ when modeling asymmetry parameters in this study.

B. CORRECTION FOR NON-ASYMPTOTIC EFFECTS

The exposition in Section 2 makes extensive use of the asymptotic approximation and related assumptions. For example, the expressions in Section 2 require incompressibility, as well as the condition that the radial wavelength is small compared both to the horizontal wavelength $\lambda_h/2\pi = r/\sqrt{\ell(\ell+1)}$ and the pressure scale height. Both assumptions are challenged for WD pulsations, which are usually localized to the outer edge of the g-mode cavity near the surface of the star, and are low-radial order at the high-frequency end. Non-asymptotic effects may be particularly important for the magnetism, whose effects are especially confined to the outer turning point of the g-mode cavity.

To investigate the effect of relaxing these assumptions, we numerically solve for the adiabatic oscillation modes using version 7.2.1 of the GYRE code (Townsend & Teitler 2013). GYRE computes both mode frequencies and fluid perturbations in the absence of assumptions about the size of the density scale height or perturbations to the gravitational potential. Equation 5 gives an asymptotic estimate of \mathcal{I} . We then compute a non-asymptotic estimate \mathcal{I} using the mode periods P and horizontal fluid displacements ξ_h from GYRE (cf. Equation 40 in Li et al. 2022):

$$\mathcal{I} = \frac{4\pi^2}{\ell(\ell+1)} P^{-2} \frac{\int_{\mathcal{R}_v}^{\ell} [\partial_r(r\xi_h)]^2 dr}{\int_{\mathcal{R}_v}^{\ell} \xi_h^2 \rho r^2 dr}. \quad (\text{B17})$$

The derivation of Equation B17 applies assumptions such as incompressibility and approximately radial wavenumber, and it ignores a surface term contribution which has been found to make a small difference (Jones et al. 1989). Nevertheless, it stops short of substituting in the full asymptotic expression for ξ_h (see the Appendix of Li et al. 2022). GYRE does not assume that the radial wavenumber is large relative to the scale height, nor does it assume the Cowling approximation. In the asymptotic limit (taking $\xi_h \propto \rho^{-1/2} r^{-3/2} N^{1/2} \sin\Phi$ with $k_r = \partial_r\Phi = \sqrt{\ell(\ell+1)}N/\omega r$), we recover Equation 5. However, \mathcal{I} may differ from its value in Equation 5 for various reasons, including corrections to the outer turning point and domination of the integrals in Equation B17 by only a single wavelength.

We bundle non-asymptotic effects into a simple, ad hoc correction factor f_{corr} , defined such that the inferred field $B_{r,\text{shift}}$ from the asymmetries is related to its asymptotic estimate by

$$f_{\text{corr}} = \frac{B_{r,\text{shift}}}{B_{r,\text{shift}}^{\text{asympt}}} = \sqrt{\frac{\mathcal{I}^{\text{asympt}}}{\mathcal{I}}} \quad (\text{B18})$$

where superscript ‘‘asympt’’ denotes the application of Equation 5 for calculating \mathcal{I} .

We find that f_{corr} is approximately described by

$$f_{\text{corr}} = f_N + (f_S - f_N) \left(\frac{2\pi}{PS_\ell} \right)_{\text{out}}^{10} \quad (\text{B19})$$

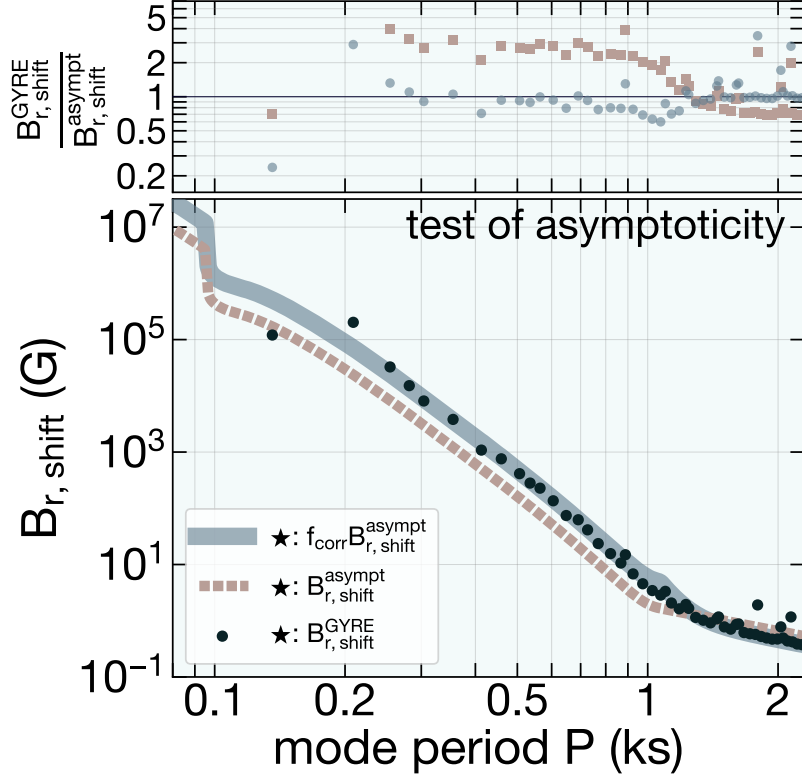


Figure 9. Model seismic magnetic field sensitivity $B_{r,\text{shift}}$, with or without the non-asymptotic correction in Equation B18 applied. *Black points* denote the non-asymptotic result using eigenfunctions calculated by GYRE (Equation B17). The *top panel* shows the ratio of the asymptotic estimate (with or without correction) to the non-asymptotic result. This figure has been extended to longer periods to emphasize the behavior of N -limited modes. The symbol \star denotes the same choice of parameters as in Figure 3.

where $f_N = 1/\sqrt{2}$ and $f_{S_\ell} = 3$, respectively, and $(2\pi/PS_\ell)_{\text{out}}$ is evaluated at the outer turning point of the mode. This form is chosen to set $f_{\text{corr}} = f_N$ for N -limited modes and $f_{\text{corr}} = f_{S_\ell}$ for S_ℓ -limited modes, with a fast but smooth transition in between the regimes enforced by an arbitrary but steep power index (10). Figure 9 shows that there is good agreement between $B_{r,\text{shift}}^{\text{GYRE}}$ (computed using GYRE eigenfunctions) and $B_{r,\text{shift}} = f_{\text{corr}} B_{r,\text{shift}}^{\text{asympt}}$. Future work should more thoroughly investigate the impact of non-asymptotic effects on seismic magnetic field measurements.